ARL-TR-7334 ● JULY 2015

US Army Research Laboratory

Flight Behavior of an Asymmetric Body through Spark Range Experiments Using Roll-Yaw Resonance for Yaw Enhancement

by Frank Fresconi, Bernard Guidos, Ilmars Celmins, and Wayne Hathaway

NOTICES

Disclaimers

The findings in this report are not to be construed as an official Department of the Army position unless so designated by other authorized documents.

Citation of manufacturer's or trade names does not constitute an official endorsement or approval of the use thereof.

Destroy this report when it is no longer needed. Do not return it to the originator.

ARL-TR-7334 ● JULY 2015

US Army Research Laboratory

Flight Behavior of an Asymmetric Body through Spark Range Experiments Using Roll-Yaw Resonance for Yaw Enhancement

by Frank Fresconi, Bernard Guidos, and Ilmars Celmins
Weapons and Materials Research Directorate, ARL

Wayne Hathaway
Arrow Tech Associates
Burlington, VT

REPORT DOCUMENTATION PAGE

Form Approved
OMB No. 0704-0188

1. REPORT DATE *(DD-MM-YYYY)*	2. REPORT TYPE	3. DATES COVERED (From - To)
July 2015	Final	October 2014–April 2015

4. TITLE AND SUBTITLE
Flight Behavior of an Asymmetric Body through Spark Range Experiments Using Roll-Yaw Resonance for Yaw Enhancement

5a. CONTRACT NUMBER

5b. GRANT NUMBER

5c. PROGRAM ELEMENT NUMBER

6. AUTHOR(S)
Frank Fresconi, Bernard Guidos, Ilmars Celmins, and Wayne Hathaway

5d. PROJECT NUMBER
AH80

5e. TASK NUMBER

5f. WORK UNIT NUMBER

7. PERFORMING ORGANIZATION NAME(S) AND ADDRESS(ES)
US Army Research Laboratory
ATTN: RDRL-WML-E
Aberdeen Proving Ground, MD 21005-5069

8. PERFORMING ORGANIZATION REPORT NUMBER
ARL-TR-7334

9. SPONSORING/MONITORING AGENCY NAME(S) AND ADDRESS(ES)

10. SPONSOR/MONITOR'S ACRONYM(S)

11. SPONSOR/MONITOR'S REPORT NUMBER(S)

12. DISTRIBUTION/AVAILABILITY STATEMENT
Approved for public release; distribution is unlimited.

13. SUPPLEMENTARY NOTES

14. ABSTRACT
The maneuvers required for guided flight are often obtained through inducing aerodynamic asymmetries. The goal of this study is to understand the flight behavior of asymmetric flight bodies. The configuration considered was a fin-stabilized projectile featuring a pair of canards representative of a class of rolling airframes with a single plane of actuating control surfaces that have recently undergone successful guided flight demonstrations. In addition to this aerodynamic asymmetry, an asymmetric mass was placed within the body. This internal asymmetry creates a trim moment and angle of attack that is amplified during free-flight as the roll rate of the body increases from zero at launch and passes through the natural yawing frequency of the projectile. Increasing the angle of attack amplitude in this manner enables analysis of a rich set of flight behaviors. Free-flight experiments were conducted on this flight body in the spark range at the Transonic Experimental Facility at the US Army Research Laboratory. Aerodynamic parameter estimation was performed on the spark range measurements using a maximum likelihood method with a body-fixed 6-degrees-of-freedom flight model. Nonlinear aerodynamic models including asymmetries in the pitching moment, normal force, and dynamic derivatives were accommodated in these techniques. Aerodynamics were compared to results obtained using computational fluid dynamics and onboard sensor techniques. Experiments also permitted analysis of the amplification factor due to roll-yaw resonance and provide a means of more easily collecting high-quality experimental data on guided projectile configurations in the future.

15. SUBJECT TERMS
guided projectile, aerodynamics, flight mechanics, asymmetry, experimental flight

16. SECURITY CLASSIFICATION OF:			17. LIMITATION OF ABSTRACT	18. NUMBER OF PAGES	19a. NAME OF RESPONSIBLE PERSON
a. REPORT	b. ABSTRACT	c. THIS PAGE	UU	64	Frank Fresconi
Unclassified	Unclassified	Unclassified			19b. TELEPHONE NUMBER (Include area code) 410-306-0794

Contents

List of Figures

List of Tables

Acknowledgments

The authors appreciate the professionalism of the crew of the Transonic Experiment Facility at the US Army Research Laboratory (ARL), John Heath, Barry Hudler, Ken Willan, Eric Miller, Bill Aubry, and Jarid Kranz in conducting the firings. The craftsmanship of Bobby Hall and the machinists at the Weapons and Materials Research Laboratory machine shop is greatly valued. Michael Minnicino, James DeSpirito, and Joseph Colburn of ARL are acknowledged for contributions to the launch, flight, and propulsion system.

1. Introduction

The motivation for this study is to better understand the flight behavior of guided projectiles. Research investments have been made for some years to enable guided, gun-launched systems[1–5] but to date have essentially only yielded the Excalibur system to the US military. A series of successful guided flight demonstrations was conducted recently for indirect fire applications with a fin-stabilized, slowly rolling airframe featuring a pair of canards that dither at the roll rate via a single-axis actuator.[6,7] This configuration has an aerodynamic asymmetry since the longitudinal plane containing the dithering canards has more normal force and a more forward center of pressure than the plane perpendicular to this canard plane.

Experiments were conducted in a variety of calibers (81 mm, 105 mm, 120 mm, and 155 mm). While the specific weapon, launch environment, flight regime, and airframe shapes were different, each overall system served as a platform to validate navigation technologies,[8–13] guidance and flight control algorithms,[14] and low-cost gun-hard actuators.[15]

Semi-empirical aeroprediction (SEAP), wind tunnel (WT), computational fluid dynamics (CFD), and onboard sensor (OS) free-flight experimental techniques were employed[16,17] throughout the design cycle for these airframes to define the outer mold line and formulate nonlinear flight models. The flight models included the aerodynamic model with input coefficient data and equations of motion. The nonlinear body-fixed 6-degrees-of-freedom equations of motion were used for system simulation[6] and hardware-in-the-loop simulation.[18] Linearized equations of motion were derived to understand how the aerodynamic asymmetry influenced flight behaviors such as stability and yawing frequencies.[19]

Ultimately, each airframe met flight requirements such as stability, maneuverability, and roll rate, but the maximum performance bounds were not specifically assessed. Studies were performed[20,21] that illustrated maneuverability increases linearly with the control force magnitude or moment arm. Of particular importance was the difference between the center-of-gravity and aerodynamic center-of-pressure locations (static margin). These studies showed a rapid increase in maneuverability as static margin goes to zero. Thus, optimizing maneuverability for this asymmetric configuration can loosely be defined as maximizing the control force and moment arm (subject to system constraints) such that the static margin is zero to within manufacturing tolerances. Dialing in a

certain static margin is problematic, however, when encountering practical variation and imperfect quantification of the center of gravity and center of pressure.

Little can be done to mitigate variation in the mass properties or aerodynamics besides tightening manufacturing tolerances. Mass properties (e.g., center of gravity) can be measured with much certainty in the laboratory. Spark ranges have been used for some time to investigate ballistic flight behavior[22–25] and are arguably the most accurate experimental aerodynamics technique due to the free-flight nature of the experiment and low measurement error. Aerodynamically asymmetric shapes such as aircraft have been analyzed in spark ranges.[26]

The goal of the present study is to use spark range techniques to obtain a highly accurate understanding of the flight behavior of a 105-mm-diameter guided projectile with aerodynamic asymmetries. Prior flight analysis[17] suggested that the launch and flight system used in this study produced relatively low launch disturbances (first maximum yaw around 1°). Launch disturbances in free-flight experiments often generate the angle of attack necessary to derive accurate aerodynamic coefficients. Devices such as muzzle breaks are modified to create asymmetric flows as the projectile exits the muzzle and ultimately increase launch disturbances. This approach can be costly in terms of hardware fabrication and range time. In the present study, an internal mass asymmetry was used to induce the desired flight motions through roll-yaw resonance. The experimental observations were used to validate linear models of flight including the amplification of yaw due to resonance. The aerodynamic coefficients and assessment of variation and uncertainty enabled a postmortem optimal maneuverability analysis of the airframe design used for the guided flight demonstration.

This report describes the materials and methods, including details of the externally and internally asymmetric projectile, spark range facility, and then the theory used for aerodynamic modeling, nonlinear and linear equations of motion, and parameter estimation process. Results are provided on the asymmetric mass property measurements, spark shadowgraphs, and complete analysis of the measured flight motions. Finally, implications of these findings on the optimality of maneuvering asymmetric projectiles are offered.

2. Materials and Methods

The airframe under investigation was fin-stabilized with a small hemispherical nosecap and von Karman ogive followed by a cylindrical section. Six clipped

delta fins were swept at 30° with a cant angle of 1.25° over the entire wetted area. Canards were emplaced near the nose, which yielded an external (aerodynamic) asymmetry. The detailed geometry is provided in Fig. 1.

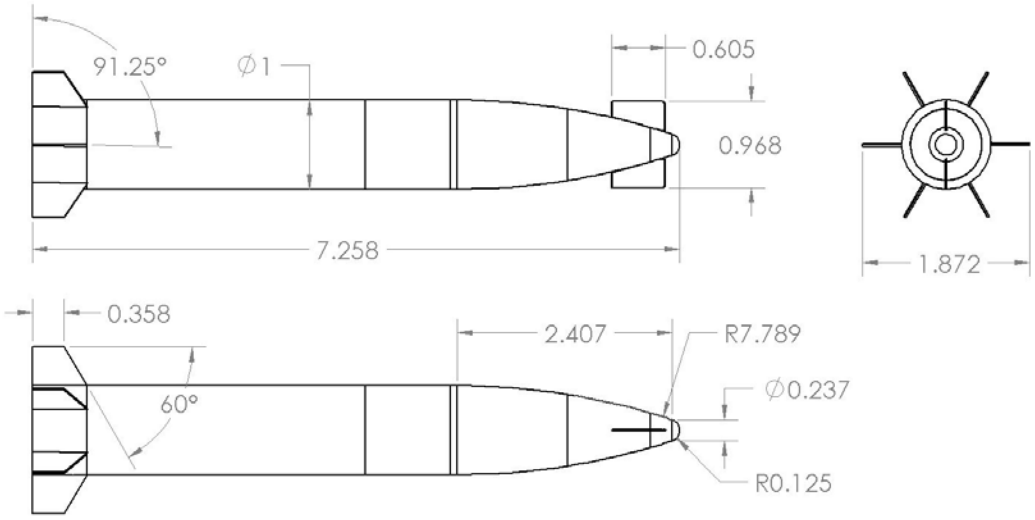

Fig. 1 Projectile dimensions (length dimensions measured in calibers)

Appreciable yaw amplitude is critical to accurately obtaining aerodynamic coefficients from free-flight experiments. Angle of attack is produced during ballistic (i.e., nonmaneuvering) flight by a variety of means: launch disturbances, atmospheric (e.g., wind) disturbances, aerodynamic or mass asymmetries, etc. Launch disturbances were small during past firings of this system and the spark range is a well-controlled environment with no wind. Mass asymmetries were chosen for inducing total angle of attack in this study since additional aerodynamic asymmetries (such as setting rigid canards to nonzero deflection angles) would alter the external shape and flow. The yaw angle of attack was augmented further through the application of resonance since the projectiles were spinning. Resonance is a phenomena whereby the angular motion is amplified by a transfer of energy from the roll motion when the yaw and roll frequencies are similar.[27–30]

A tungsten mass insert was designed for the projectiles. This mass was placed in the forward section of the body to maintain static stability. Cutaways are shown of the mass asymmetry in Fig. 2. In the top illustration the tungsten insert is shown as a dark-shaded mass along the bottom of the projectile forward of the intersection of the ogive and cylindrical sections. The bottom rendering shows a view from the rear of the airframe looking out toward the nose. The 2 (subcaliber) canards in the vertical plane and 6 fins are evident. The pie-shaped wedge to the right is the mass insert. A body-fixed coordinate system is introduced with the x_B

axis proceeding along the longitudinal axis out the projectile nose, y_B axis along the center of the mass insert, and z_B axis completing a right-hand system and lying in the canard plane.

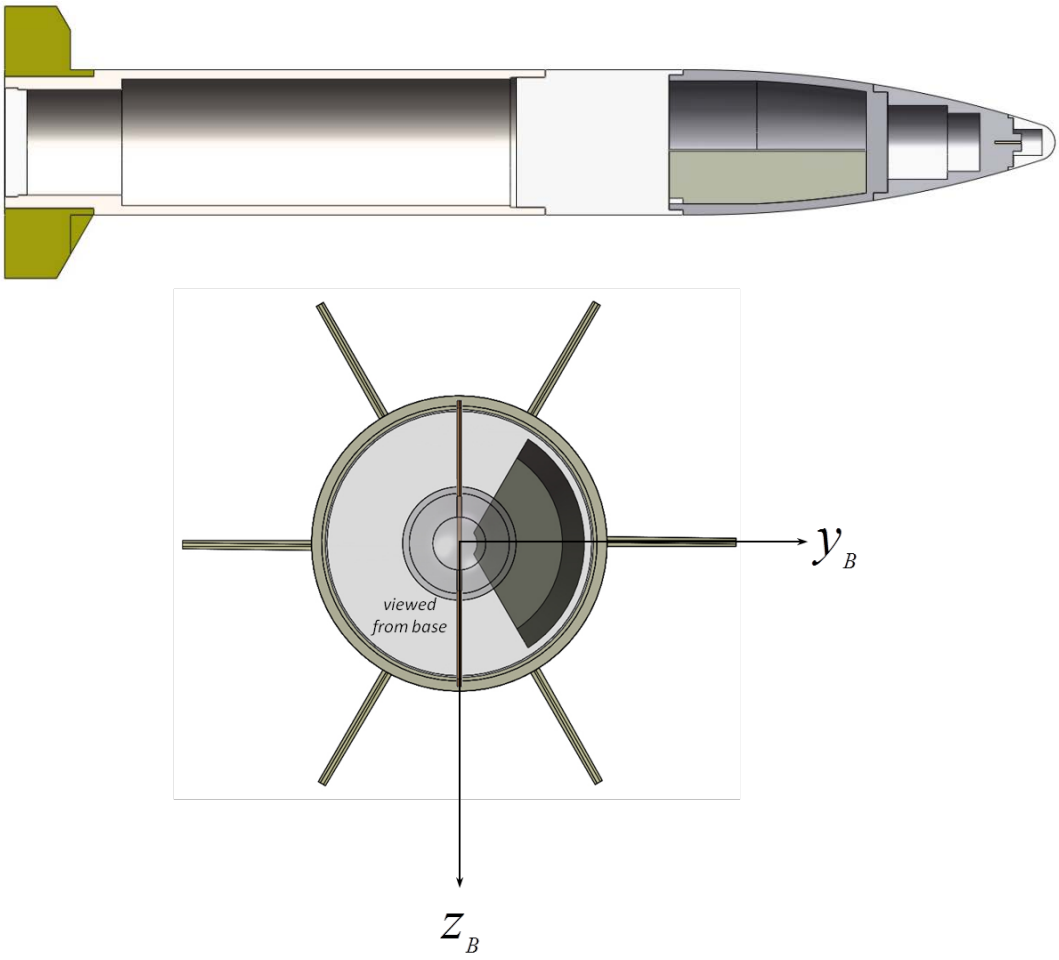

Fig. 2 Cutaway of projectile with internal asymmetry: longitudinal (top) and axial (bottom)

The projectile was assembled within an obturator-pusher plate-sabot assembly and launched from a smoothbore 8-inch gun. Further details, to include the launch package, gun, and firing data, are provided in Celmins[31] and Appendix A.

The spark range facility at the Transonic Experimental Facility is shown looking toward the entry portal in Fig. 3. The gun is positioned outside, preventing the muzzle blast, sabot petals, and other launch residue from interfering with data acquisition. The enclosed range is instrumented with 25 spark stations in 5 groups of 5 each over an entire distance of approximately 200 m. Each spark station consists of a light screen trigger, 2 spark sources, and 2 cameras. The trigger, spark source, and one camera are contained in the floor pits of Fig. 3. The other

camera and spark source are mounted on the wall to the right in Fig. 3. The panels that serve as a background for the cameras on the ceiling are on the left in the figure. A wire system equipped with fiducial beads near the panels runs throughout the range to provide accurate position information.

Fig. 3 Spark range facility

The range is darkened prior to firing. When the projectile passes through the plane of the light screen, a high-intensity light source is triggered. Each camera captures a focused image of the projectile's shadow (i.e., shadowgraph) in the 2 orthogonal planes. The shadowgraphs provide projectile images that are interpreted along with the fiducial bead system to calculate the projectile center-of-gravity position ($[x \quad y \quad z]$) and Euler angles ($[\phi \quad \theta \quad \psi]$). The roll angle ($\phi$) was obtained by measuring the locations of small, square notches cut into the trailing edge of one fin and the spanwise edge of another fin. Trigger times and range meteorological conditions were also recorded. Flow-field patterns are often apparent in the shadowgraphs as well.

A physical model was used to represent the aerodynamic forces and moments on the body. The aerodynamic model is primarily concerned with relating airframe states such as angle of attack or pitch rate to aerodynamic forces and moments. Figure 4 shows a schematic of the airframe with the body-fixed coordinate system. All quantities (e.g., forces, velocities) for the aerodynamic model are computed in the body-fixed coordinate system.

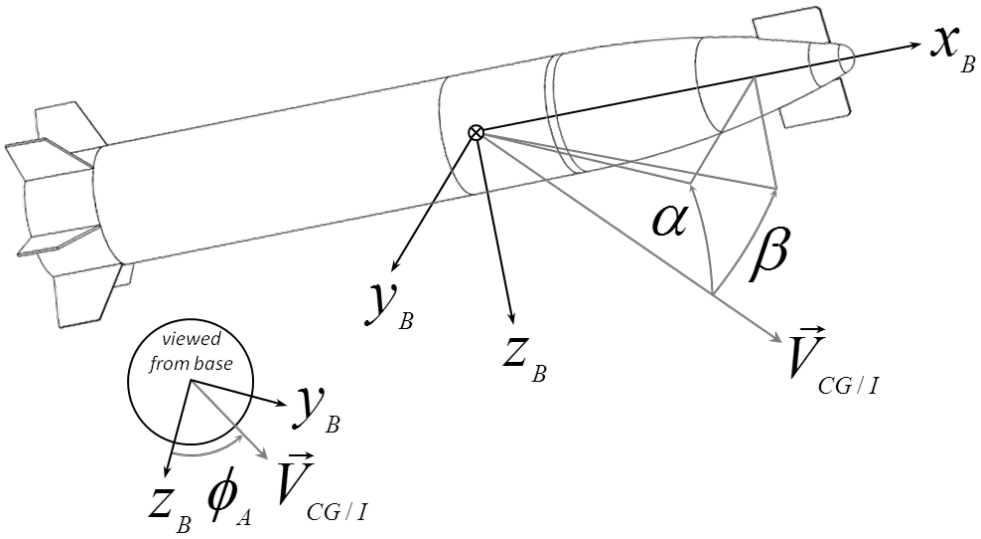

Fig. 4 Coordinate system definitions for aerodynamic angles

The body velocity ($[u \quad v \quad w]$) components depicted in this figure are used to determine the angle of attack (pitch plane), angle of sideslip (yaw plane), total angle of attack, and aerodynamic roll angle. These relationships are defined in Eqs. 1–4.

$$\alpha = asin\left[\frac{w}{\sqrt{u^2+v^2+w^2}}\right] . \tag{1}$$

$$\beta = asin\left[\frac{v}{\sqrt{u^2+v^2+w^2}}\right] . \tag{2}$$

$$\bar{\alpha} = \sqrt{\alpha^2 + \beta^2} . \tag{3}$$

$$\phi_A = atan\left[\frac{v}{w}\right] . \tag{4}$$

Aerodynamic forces have 3 components as given in Eqs. 5–7. The axial component includes linear (C_{X_0}) and nonlinear ($C_{X_{\bar{\alpha}^2}}$ i.e., with angle of attack) static terms. Nonlinear terms were neglected in the lateral components and dynamic terms (e.g., function of roll rate) were neglected throughout since they were not found to be necessary in the analysis. Aerodynamic asymmetry is accommodated in this model since the lateral normal force derivatives (e.g., C_{Y_β}, C_{Z_α}) are different. The canards are perpendicular to the y_B axis, therefore $C_{Y_\beta} > C_{Z_\alpha}$. Symbols in parenthesis indicate functional form of aerodynamic coefficients. The dynamic pressure is $Q = \frac{1}{2}\rho V^2$ and aerodynamic reference area is $S = \frac{\pi}{4}D^2$, where D is the projectile diameter and V is the total velocity.

$$\mathrm{X} = -QS\left[C_{X_0}(M) + C_{X_{\bar{\alpha}^2}}(M)\sin^2\bar{\alpha}\right] \ . \tag{5}$$

$$Y = -QSC_{Y_\beta}(M)\sin\beta \ . \tag{6}$$

$$Z = -QSC_{Z_\alpha}(M)\sin\alpha \ . \tag{7}$$

Aerodynamic moment equations provided in Eqs. 8–10 feature static and dynamic (i.e., dependent on angular rates $[p \quad q \quad r]$) terms. The roll moment includes static (C_{l_0} e.g., roll production due to fin cant) and damping (C_{l_p}) terms. Trim (C_{m_0}, C_{n_0}) and first order (C_{m_α}, C_{n_β}) terms are retained for the pitching moment. Asymmetries are present for the pitching moment and pitch damping moment (C_{m_q}, C_{n_r}) terms. A symmetric static side moment (C_{n_α}) was included in the aerodynamic model. Dynamic side moments were not found necessary in the analysis. The lateral moments account for a center of gravity ($\overrightarrow{CG_N}$), which has been shifted from the reference center of gravity ($\overrightarrow{CG_{N,A}}$) used to obtain the initial aerodynamic data ($\vec{\Delta}_{\mathrm{CG}} = [CG_{X,N} \quad CG_{Y,N} \quad CG_{Z,N}] - [CG_{X,R} \quad CG_{Y,R} \quad CG_{Z,R}]$). The origin of the center-of-gravity vector is at the nose and is given in units of calibers.

$$\begin{aligned} L = QSD\left[C_{l_0}(M) + C_{l_p}(M)\frac{pD}{2V}\right] + Z\left(CG_{Y,N} - CG_{Y,R}\right)D \\ -Y\left(CG_{Z,N} - CG_{Z,R}\right)D \quad . \end{aligned} \tag{8}$$

$$\begin{aligned} M = QSD\left[C_{m_0}(M) + C_{m_\alpha}(M)\sin\alpha + C_{m_q}(M)\frac{qD}{2V} + C_{n_\alpha}(M)\sin\beta\right] \\ +X\left(CG_{Z,N} - CG_{Z,R}\right)D - Z\left(CG_{X,N} - CG_{X,R}\right)D \quad . \end{aligned} \tag{9}$$

$$\begin{aligned} N = QSD\left[-C_{n_0}(M) - C_{n_\beta}(M)\sin\beta + C_{n_r}(M)\frac{rD}{2V} + C_{n_\alpha}(M)\sin\alpha\right] \\ +Y\left(CG_{X,N} - CG_{X,R}\right)D - X\left(CG_{Y,N} - CG_{Y,R}\right)D \quad . \end{aligned} \tag{10}$$

This aerodynamic model is used in the equations of motion for flight. Figure 5 introduces the relationship between the body reference frame (with body-fixed coordinate system) where aerodynamic computations take place and the inertial reference frame (with Earth coordinate system $[x_E \quad y_E \quad z_E]$) where Newton's second law is applied. Euler angles transform between quantities in the body-fixed and Earth coordinates.

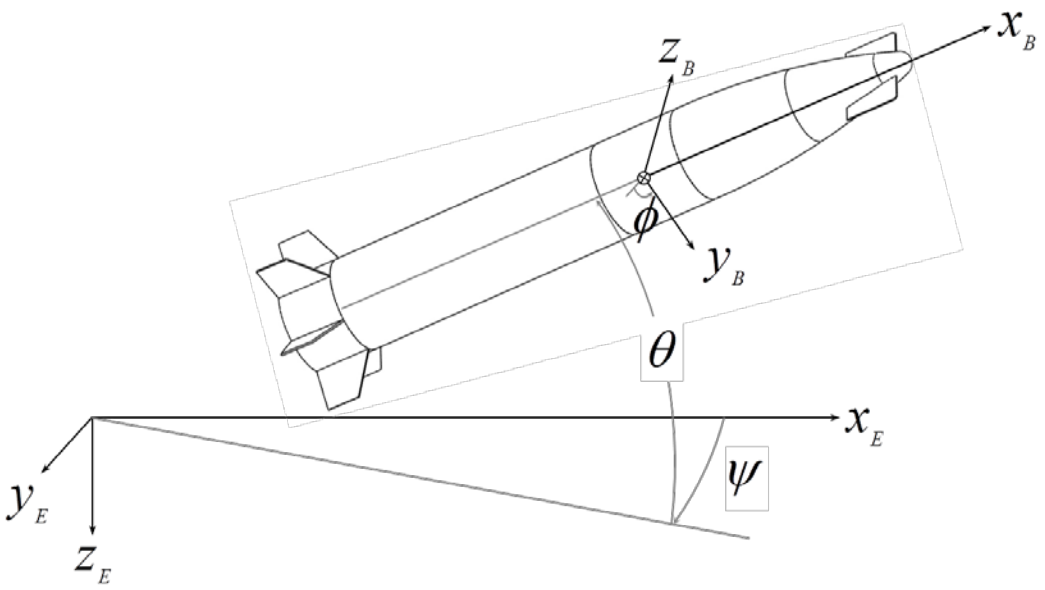

Fig. 5 Coordinate system definitions for Euler angles

The equations for the kinematics and dynamics of translation and rotation are shown in Eqs. 11–14.[27–29,32] The aerodynamic model appears in the dynamics of Eqs. 13 and 14 along with the mass (m) and moment of inertia tensor ($\vec{I}$). These equations are implemented numerically for time integration and represent the 6-degrees-of-freedom flight model.

$$\begin{bmatrix}\dot{x}\\ \dot{y}\\ \dot{z}\end{bmatrix} = \begin{bmatrix} c_\theta c_\psi & s_\phi s_\theta c_\psi - c_\phi s_\psi & c_\phi s_\theta c_\psi + s_\phi s_\psi \\ c_\theta s_\psi & s_\phi s_\theta s_\psi + c_\phi c_\psi & c_\phi s_\theta s_\psi + s_\phi c_\psi \\ -s_\theta & s_\phi c_\theta & c_\phi c_\theta \end{bmatrix} \begin{bmatrix} u \\ v \\ w \end{bmatrix}. \tag{11}$$

$$\begin{bmatrix}\dot{x}\\ \dot{y}\\ \dot{z}\end{bmatrix} = \begin{bmatrix} c_\theta c_\psi & s_\phi s_\theta c_\psi - c_\phi s_\psi & c_\phi s_\theta c_\psi + s_\phi s_\psi \\ c_\theta s_\psi & s_\phi s_\theta s_\psi + c_\phi c_\psi & c_\phi s_\theta s_\psi + s_\phi c_\psi \\ -s_\theta & s_\phi c_\theta & c_\phi c_\theta \end{bmatrix} \begin{bmatrix} u \\ v \\ w \end{bmatrix}. \tag{12}$$

$$\begin{bmatrix}\dot{u}\\ \dot{v}\\ \dot{w}\end{bmatrix} = \frac{1}{m}\begin{bmatrix} X - g s_\theta \\ Y + g s_\phi c_\theta \\ Z + g c_\phi c_\theta \end{bmatrix} - \begin{bmatrix} 0 & -r & q \\ r & 0 & -p \\ -q & p & 0 \end{bmatrix} \begin{bmatrix} u \\ v \\ w \end{bmatrix}. \tag{13}$$

$$\begin{bmatrix}\dot{p}\\ \dot{q}\\ \dot{r}\end{bmatrix} = \vec{I}^{-1}\begin{bmatrix} L \\ M \\ N \end{bmatrix} - \vec{I}^{-1}\begin{bmatrix} 0 & -r & q \\ r & 0 & -p \\ -q & p & 0 \end{bmatrix} \vec{I} \begin{bmatrix} p \\ q \\ r \end{bmatrix}. \tag{14}$$

Parameter estimation was conducted on the spark range data to obtain the aerodynamic coefficients. A maximum likelihood method was applied.[33–37] This technique seeks to minimize the likelihood function given in Eq. 15 to find model parameters.

$$\mathcal{L} = \frac{1}{(2\pi)^{\frac{N_M}{2}}\sqrt{\vec{\mathbb{R}}}} exp\left(-\frac{1}{2}\vec{\epsilon}^T\vec{\mathbb{R}}^{-1}\vec{\epsilon}\right). \tag{15}$$

The residuals are the difference between measurements and flight model calculations ($\vec{\epsilon} = \vec{x}_M - \vec{x}_C$). The spark range provides center-of-gravity position and Euler angle measurements ($\vec{x}_M = [x \quad y \quad z \quad \phi \quad \theta \quad \psi]$). The residual covariance is a measure of the expected errors ($\vec{\mathbb{R}} = E[\vec{\epsilon}\vec{\epsilon}^T]$). A major strength of the spark range is the accuracy of the measurements. Typically, the spark range uncertainty is 0.003 m in position, 0.1° in pitch/yaw, and 2.5° in roll. The uncertainty in roll for this study is around 5° due to the difficulty in measuring roll for this configuration. The number of measurement samples (N_M) is the number of spark range stations where data were collected. The position and Euler angles were calculated ($\vec{x}_C$) using the aerodynamic model and equations of motion outlined earlier.

The parameter estimation adjusts the aerodynamic coefficients and initial conditions so that the theoretical calculations of position and Euler angles better match the measurements. The following aerodynamic and initial conditions parameter vector was used for this study.

$$\begin{aligned}\vec{\theta} = \big[&C_{x_0} \quad C_{y_\beta} \quad C_{z_\alpha} \quad C_{l_0} \quad C_{l_p} \quad C_{m_0} \quad C_{n_0} \quad C_{m_\alpha} \quad C_{m_\beta} \quad C_{n_\alpha} \\ &x_0 \quad y_0 \quad z_0 \quad \phi_0 \quad \theta_0 \quad \psi_0 \quad u_0 \quad v_0 \quad w_0 \quad p_0 \quad q_0 \quad r_0\big].\end{aligned} \tag{16}$$

Initial guesses of these parameters were used for propagating the models forward in time. A Newton-Raphson method was implemented to optimize the likelihood function when times were reached where spark range measurements were available. The residual and Jacobian ($\frac{\partial \vec{x}_C}{\partial \vec{\theta}}$) were calculated.

$$\frac{\partial \vec{x}_C}{\partial \vec{\theta}} = \begin{bmatrix} \frac{\partial x_{C_1}}{\partial \theta_1} & \frac{\partial x_{C_2}}{\partial \theta_2} & \cdots \\ \frac{\partial x_{C2}}{\partial \theta_1} & \ddots & \vdots \\ \vdots & \cdots & \frac{\partial x_{C_{N_M}}}{\partial \theta_{N_P}} \end{bmatrix}. \tag{17}$$

The number of parameters is N_P. It was necessary to carry forward integration in time with perturbed parameters for Jacobian calculation via forward differencing. When the end of a time series of data was reached, parameters were corrected and applied to update the parameter estimates.

$$\Delta\vec{\theta} = \left(\sum_{i=1}^{N_M} \frac{\partial \vec{x}_{C,i}}{\partial \vec{\theta}}^T \vec{\mathbb{R}}^{-1} \frac{\partial \vec{x}_{C,i}}{\partial \vec{\theta}}\right)^{-1} \sum_{i=1}^{N_M} \frac{\partial \vec{x}_{C,i}}{\partial \vec{\theta}}^T \vec{\mathbb{R}}^{-1}\vec{\epsilon}_i \ . \tag{18}$$

$$\vec{\theta}^{j+1} = \vec{\theta}^j + \Delta\vec{\theta} \ . \tag{19}$$

This entire loop was iterated with the updated parameters until meeting the convergence criterion. This technique yielded the optimal parameter estimates and calculated response over the entire measurement history.

Linear systems theory has been applied with much success to understand ballistic flight behavior.[19,23,27–29] For a symmetric projectile, the expression for the fast and slow mode yawing frequencies ($\omega_{F,S}$) based on linear theory[27] is given in Eq. 20.

$$\omega_{F,S} = \frac{p_{ss} I_A}{2I_T}\left[1 \pm \sqrt{1 - \frac{\pi \rho I_T D^3 C_{m_\alpha}}{2I_A^2 \left(\frac{p_{ss}}{V}\right)^2}}\right] . \tag{20}$$

In this equation, I_A is the axial moment of inertia, I_T is the transverse moment of inertia, and $p_{ss} = \frac{-2VC_{l_0}}{D\left(C_{l_p} + \frac{I_A}{mD^2} C_{X_0}\right)}$ is the steady state roll rate. Cooper et al.[19] showed that the yawing frequencies do not change appreciably for the purposes of this study when explicitly considering the aerodynamic asymmetry in the linearization.

Another important linear theory result for this study is the amplification factor. The amplification factor predicts the growth in yaw when a trim is present as the projectile experiences roll-yaw resonance. The equation for the amplification factor (ξ,[28]) is

$$\xi = \frac{\rho S D C_{m_\alpha}}{2I_T \sqrt{\left[\left(\frac{p_{ss}}{V} - \omega_F\right)\left(\frac{p_{ss}}{V} - \omega_S\right) - \lambda_F \lambda_S\right]^2 + \left[\lambda_S\left(\frac{p_{ss}}{V} - \omega_F\right) + \lambda_F\left(\frac{p_{ss}}{V} - \omega_S\right)\right]}} . \tag{21}$$

Here, λ_F is the fast mode damping rate and λ_S is the slow mode damping rate.

3. Results

Internally symmetric and asymmetric models were machined and the mass properties were measured on high-precision instruments at the Transonic Experimental Facility. The measurement procedures to obtain the mass, center-of-gravity location, and moment-of-inertia tensor for models with internal asymmetry are outlined in Appendix B. The results for the symmetric and asymmetric internal configuration were averaged to produce the results in Table 1. The center of gravity with the tungsten mass offset was 4.5 mm off the axis of symmetry and had cross-axis moment of inertia on the same order of magnitude as the axial moment of inertia. The reference diameter was 0.1047 m and the overall length of the models was 0.76 m. Table 1 also provides the shot numbers of the internally symmetric and internally asymmetric configurations.

Table 1 Measured mass properties

Internal Configuration	Shots (TRN)	m (kg)	CG_X (m from nose)	CG_Y (m from nose)	I_{XX} (kg-m^2)	I_{YY} (kg-m^2)	I_{ZZ} (kg-m^2)	I_{YZ} (kg-m^2)
Symmetric	39045 39363	19.127	0.4012	0.0	0.033205	0.736000	0.736000	0.0
Asymmetric	39043 39044 39319 39320 39360 39361 39362	23.086	0.3687	0.0045	0.036760	0.864575	0.865975	0.015175

The models were fired through the spark range as detailed above at a low transonic Mach number (~0.9). A representative shadowgraph of an airframe pitched up is given in Fig. 6. The body has rolled to an orientation such that the ogive-mounted canard planform is clearly visible. The fins are also evident along with some of the wake aft of the base. A sister image was captured in the orthogonal plane at this station. The fiducial (not shown) was used with the projectile image to calculate the center-of-gravity position and Euler angles. This process was repeated at all spark stations for each shot.

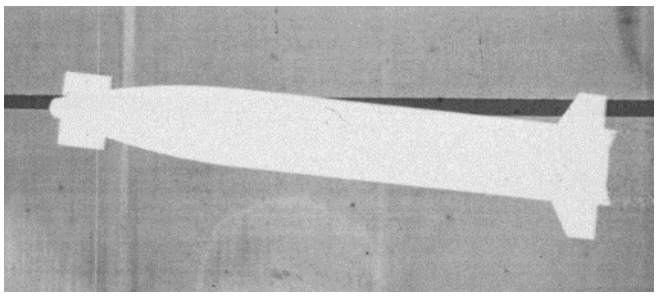

Fig. 6 Shadowgraph of model during free-flight experiment

The spark range and mass property data were used in the nonlinear parameter estimation technique outlined above. An example of this analysis is presented for TRN39362. This flight possessed a mass asymmetry. The experimental and calculated angular motion (pitch/yaw Euler angles) is given in Fig. 7. Data were collected at 23 stations. In the upper plot, the solid curve and filled dots represent the pitch angle and the dashed curve and hollow dots are for the yaw angle. The model undergoes approximately 3 cycles of angular motion over the course of the instrumented range. The pitch and yaw angles are initially about 2° or less and the amplitude grows with downrange distance to about 6°. The lower plot shows that the projectile nose turns down and to the right after launch. The nose traces a widening, elliptical path later in flight.

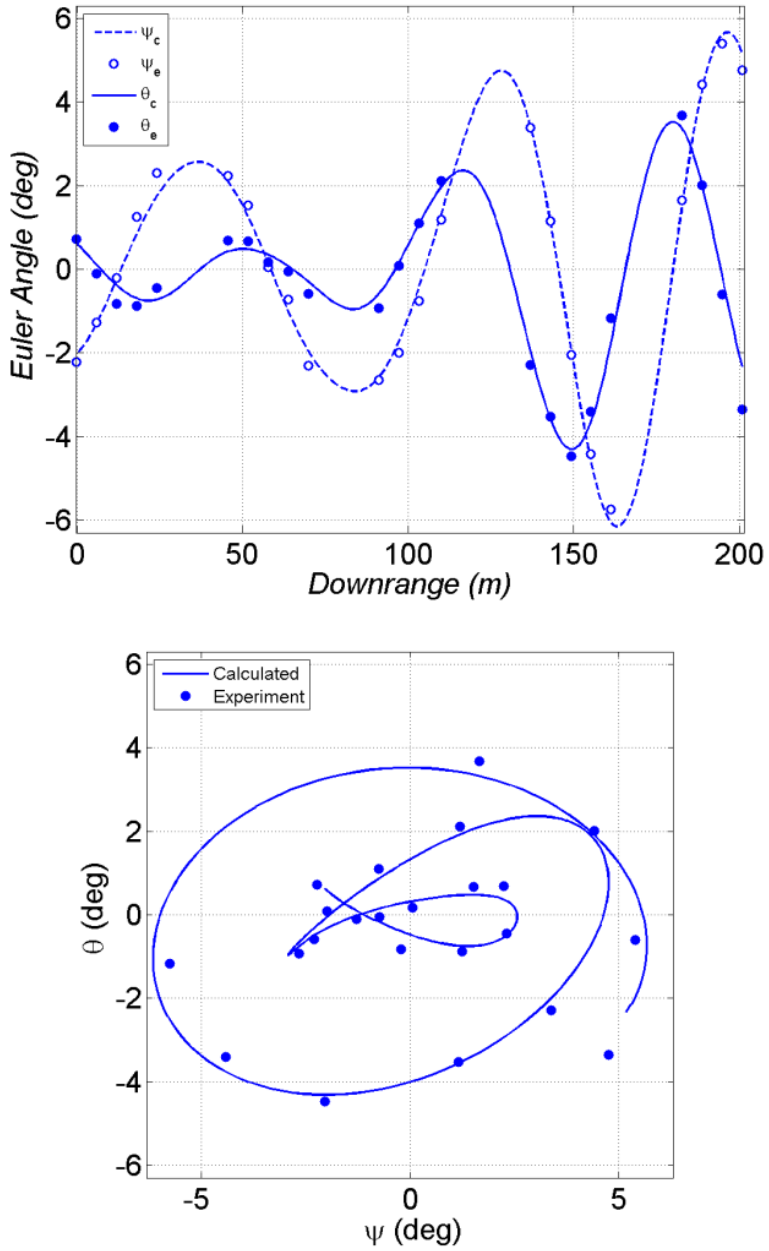

Fig. 7 Angular motion for TRN39362

The calculated and experimental center-of-gravity motion for TRN39362 is presented in Fig. 8. The solid lines and filled circles are for the vertical direction and the dashed lines and open circles are for the horizontal direction. The sign of the data in the vertical direction has been swapped to better visualize the typical ballistic trajectory arc. The horizontal direction flies off the line of fire mainly due to aerodynamic jump.[26,28] Oscillation in the center of gravity is due to the

change in normal force with angle of attack throughout the flight. The extreme accuracy of the spark range measurements (typically 0.003 m) enables aerodynamic normal force estimation.

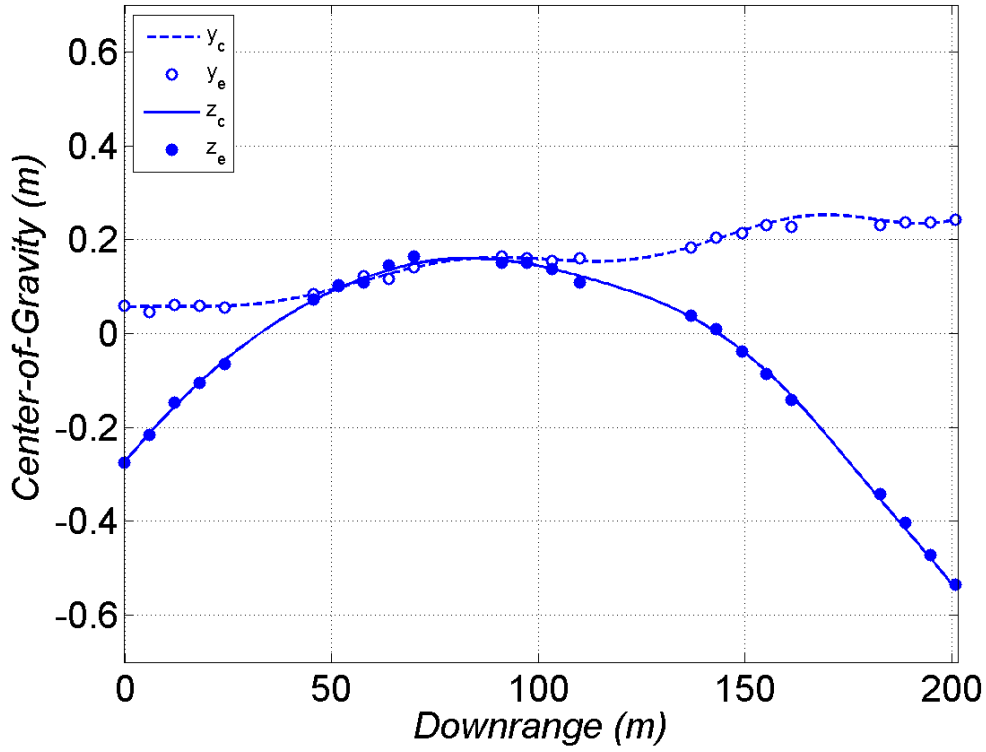

Fig. 8 Center-of-gravity motion for TRN39362

The rolling motion for TRN39362 is provided in Fig. 9. The projectile was loaded into the smoothbore gun at approximately $\phi = -90°$ (mass insert up when viewed from behind gun). The rate of change in the roll angle increases throughout the range; steady-state roll rate was not reached. The projectile experienced about 3 revolutions by the range exit.

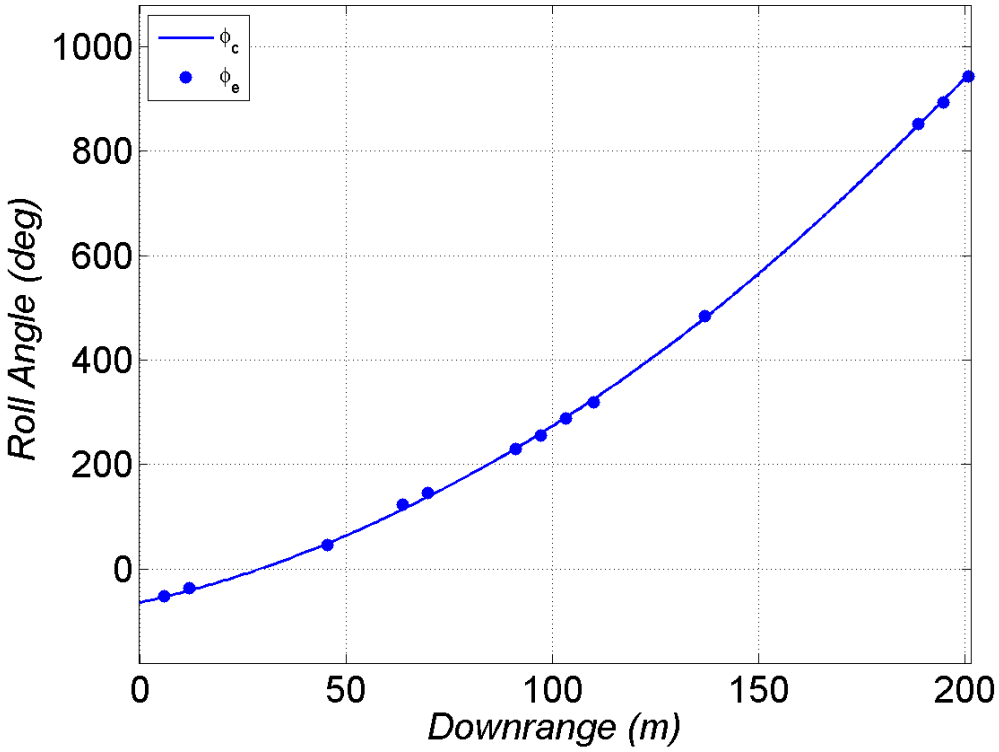

Fig. 9 Roll motion for TRN39362

The flight of the internally symmetric models had some significant differences from the mass asymmetry models. The angular motion for TRN39363, which was internally symmetric, is shown in Fig. 10. Similar to Fig. 7, about 3 cycles of motion were recorded. The pitch and yaw angles only reached a little over 1°, though. Accurate aerodynamic parameter estimation is more difficult as the flight dynamics are weakly perturbed and the yawing amplitude approaches the measurement uncertainty. The right-most plot in Fig. 10 demonstrates that the angular motion remains mainly within 1° of the line of fire over the course of the flight.

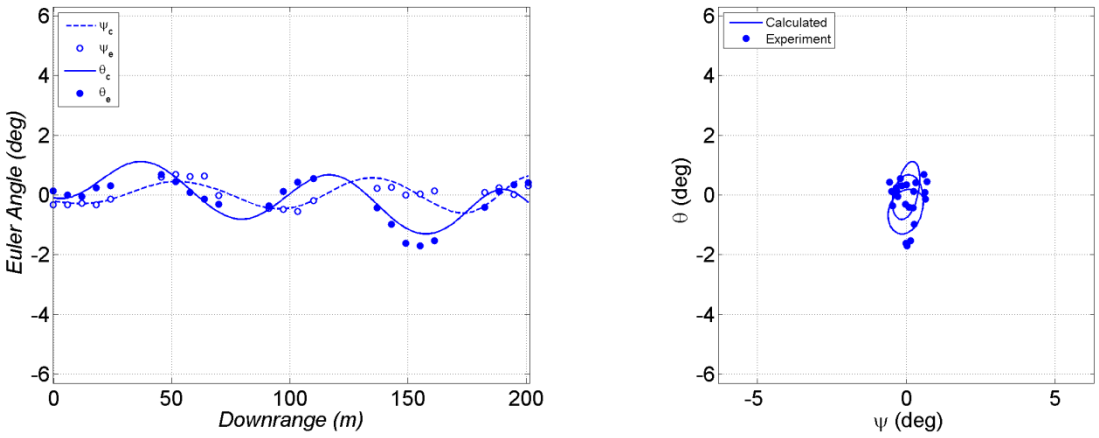

Fig. 10 Angular motion for TRN39363

The center-of-gravity motion for TRN39363 is given in Fig. 11. Again, the trajectory arc is apparent in the vertical direction. Little oscillation is observed in the horizontal data due to the low amplitude angular motion, which makes accurate estimation of aerodynamic normal force more difficult. Without the mass asymmetry, the projectile flies at such low total angle of attack as to approach a point-mass trajectory. In this limit, zero-yaw axial force and roll moments are the only aerodynamic parameters that can be determined with reasonable accuracy.

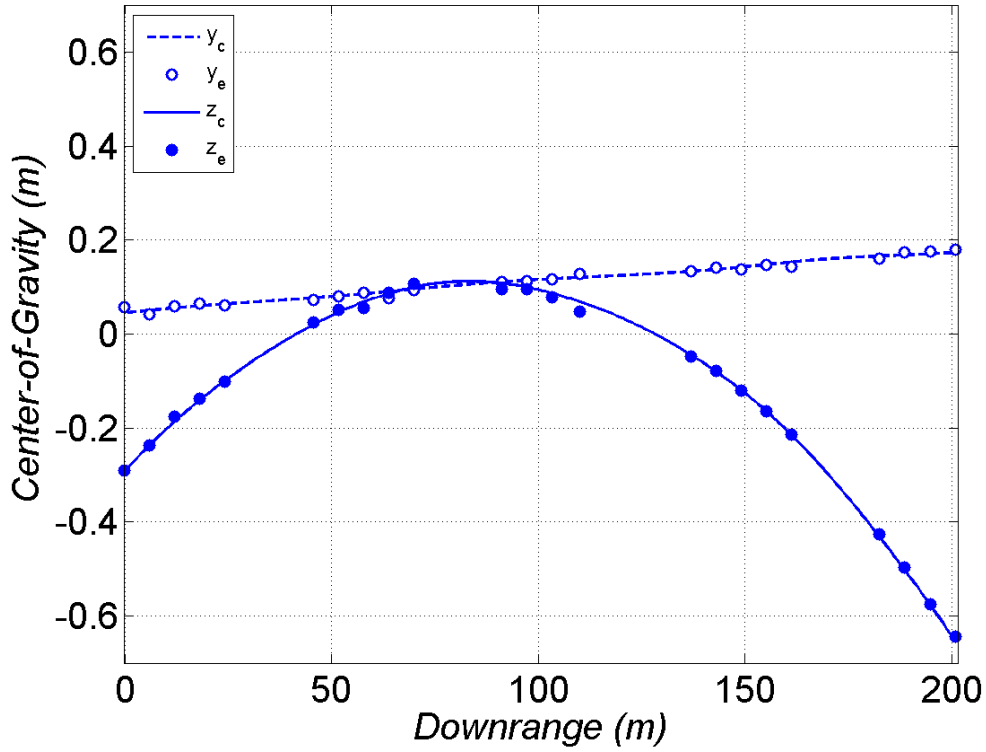

Fig. 11 Center-of-gravity motion for TRN39363

The lack of angular motion does not significantly influence the rolling motion. Figure 12 gives the roll motion for TRN39363. The projectile was loaded and launched near $\phi = -90°$ and the roll-up history is similar to that shown for TRN39362.

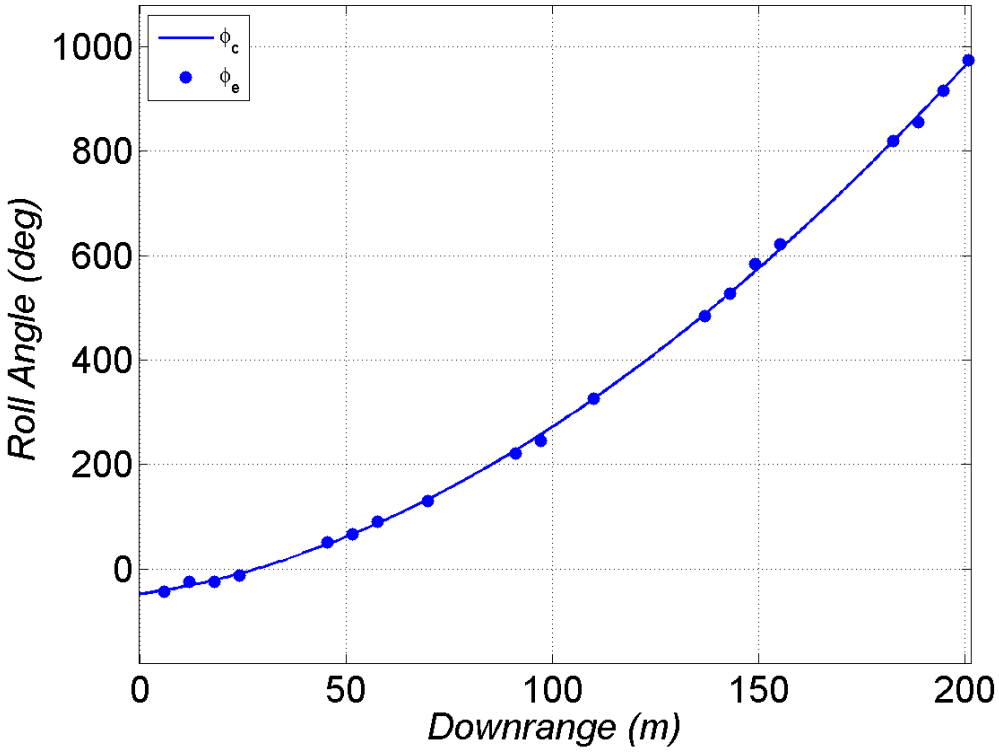

Fig. 12 Roll motion for TRN39363

Nine flights were analyzed. The error between model predictions and experiments was usually within the measurement uncertainty. The details of the calculated and experimental motion for the remaining flights are provided in Appendix C. Matching calculations to the experimental data permits reconstruction of all flight states and estimation of all parameters (aerodynamic coefficients and initial conditions). Table 2 collects the Mach, maximum total angle of attack, initial pitch rate, initial yaw rate, aerodynamic trim angles in the pitch (ζ_α) and yaw (ζ_β) planes, and the trim due to mass asymmetry trim (ζ_M, yaw plane only) for each flight. The initial pitch and yaw rates are in fixed-plane coordinates, which is essentially the body-fixed coordinates in Fig. 4 with the y_B axis always parallel to the ground. In this system, positive q would rotate the nose up and positive r would rotate the nose right when viewed from behind the gun. The aerodynamic trim angles are calculated as $\zeta_\alpha = \frac{C_{m_0}}{C_{m_\alpha}}$ and $\zeta_\beta = \frac{-C_{n_0}}{C_{n_\beta}}$. A simple free-body diagram permits derivation of the mass trim as $\zeta_M = \frac{\Delta_{CG,Y}}{D}\frac{C_{X_0}}{C_{Y_\beta}}$. Inspection of Table 2 shows a variation in Mach of about 0.05. The maximum total angle of attack correlates with the internal model configuration.

Table 2 Mach, maximum total angle of attack, initial pitch and yaw rates, aerodynamic and mass trim angles

TRN	Mach	$\bar{\alpha}_{max}$	q_0 (rad/s)	r_0 (rad/s)	ζ_α (°)	ζ_β (°)	ζ_M (°)
39043	0.906	4.402	–0.366	0.250	0.240	–0.253	–0.134
39044	0.910	5.715	–0.220	0.261	–0.222	0.186	–0.158
39045	0.909	1.383	–0.138	0.055	0.067	–0.138	0.000
39319	0.862	4.427	0.046	0.348	–0.516	–1.089	–0.199
39320	0.889	2.950	–0.838	0.126	0.162	–0.313	–0.134
39360	0.881	3.656	–0.448	0.819	0.000	0.755	–0.238
39361	0.885	4.916	–0.376	–0.211	0.063	0.274	–0.146
39362	0.874	6.268	–0.423	0.413	0.331	–0.029	–0.175
39363	0.865	0.892	–0.089	–0.066	0.000	0.125	0.000

The initial pitch and yaw rates (i.e., tip-off) are dictated by complicated processes including in-bore balloting and sabot discard. Tip-off due to balloting is likely small in this study due to the large contact surface of the plastic sabot against the smoothbore gun.

The model asymmetry also induces initial angular rate. The axial force acts at the aerodynamic center of pressure but the center of gravity is shifted 4.5 mm off the axis of symmetry, which creates a moment. This moment is mathematically expressed in the $X\left(CG_{Y,N} - CG_{Y,R}\right)D$ term in Eq. 10 and ultimately produces angular rate.

To verify this concept, numerical experiments were conducted on this airframe with the internal asymmetry in the 6-degrees-of-freedom model with the static roll moment set to zero (e.g., zero roll rate). The projectile was launched with no initial tip-off and a negative pitch rate (i.e., nose down) was produced after launch due to the offset mass. Another simulation was conducted with rolling motion (static roll moment enabled) and zero tip-off. The body again experienced a negative pitch rate soon after launch; however, the addition of the roll dynamics also yielded a positive yaw rate.

Trends are evident in the tip-off data in Table 2. The majority of the flights, especially with mass asymmetry, are tipped nose down and to the right when viewed from behind the gun. These data along with the numerical experiments suggest internal configuration may contribute the most to the early angular rate, followed by the sabot discard.

Trims are critical in the amplification of total angle of attack when experiencing roll-yaw resonance. The aerodynamic trims in both planes given in Table 2 are usually fractions of a degree. These values are expected as in practice it is difficult to construct a model launched from a gun with perfect external symmetry. The trim due to mass asymmetry is consistently around –0.1° to –0.2°.

A comparison of aerodynamic and mass trims demonstrates that both trims are usually around the same order of magnitude.

The total angle-of-attack history resulting from matching the experimental data for each flight is provided in Fig. 13. The mass asymmetry models are the solid blue lines and the internally symmetric models are the dashed black lines. Higher total angle of attack is undoubtedly attained with the internal asymmetries. The blue series of curves features higher initial total angle of attack and near halfway through the range the total angle-of-attack magnitude increases to as much as 6° or so. Meanwhile, the internally symmetric models are launched near 1° and total angle of attack does not cross 1° throughout the majority of the flights. Clearly, the internal configuration affects the launch disturbances and the total angle of attack.

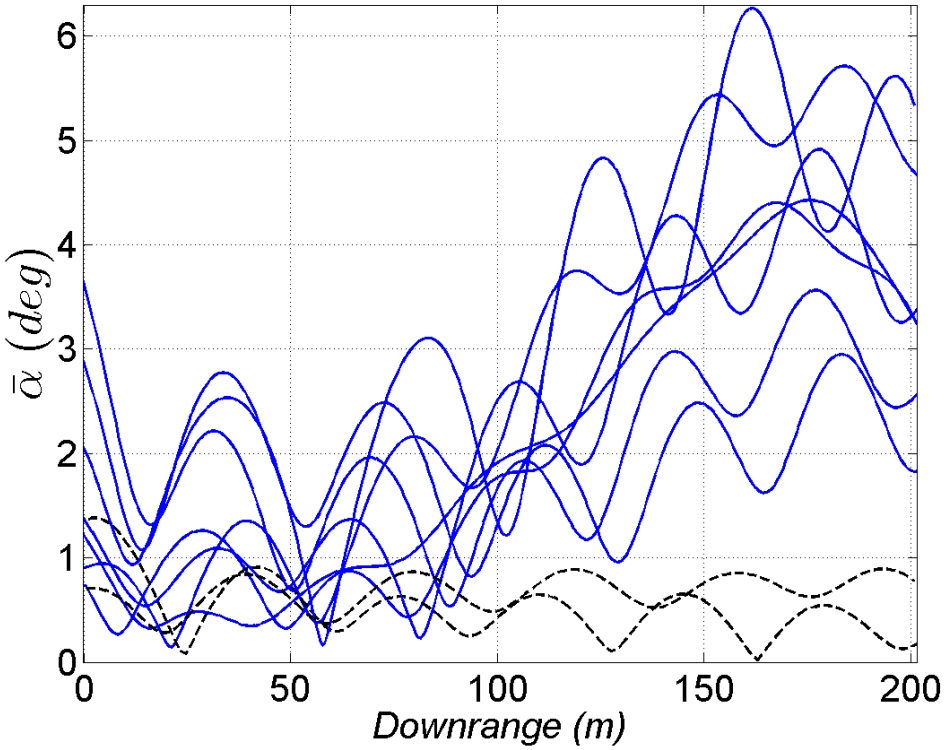

Fig. 13 Total angle-of-attack history for all flights

The flights of TRN39362 and TRN39363 are again isolated to better understand the cause of higher yaw magnitude for the internal asymmetries. Figure 14 shows the total angle of attack, calculated roll rate, yawing frequency (Eq. 20), and amplification factor (Eq. 21) for TRN39362. The roll rate increases almost linearly from zero at the muzzle to about 6.5 Hz at range exit. The yaw rate is about 4.5 Hz so the airframe definitely experiences roll-yaw resonance about

120 m downrange from the first spark station. The amplification factor is near one at the range entrance and peaks near the range midpoint. Total angle of attack remains around 2°–3° for the first half of the range and begins to increase appreciably to over 6° after the middle of the range. The linear theory predictions seem to capture the experimental results.

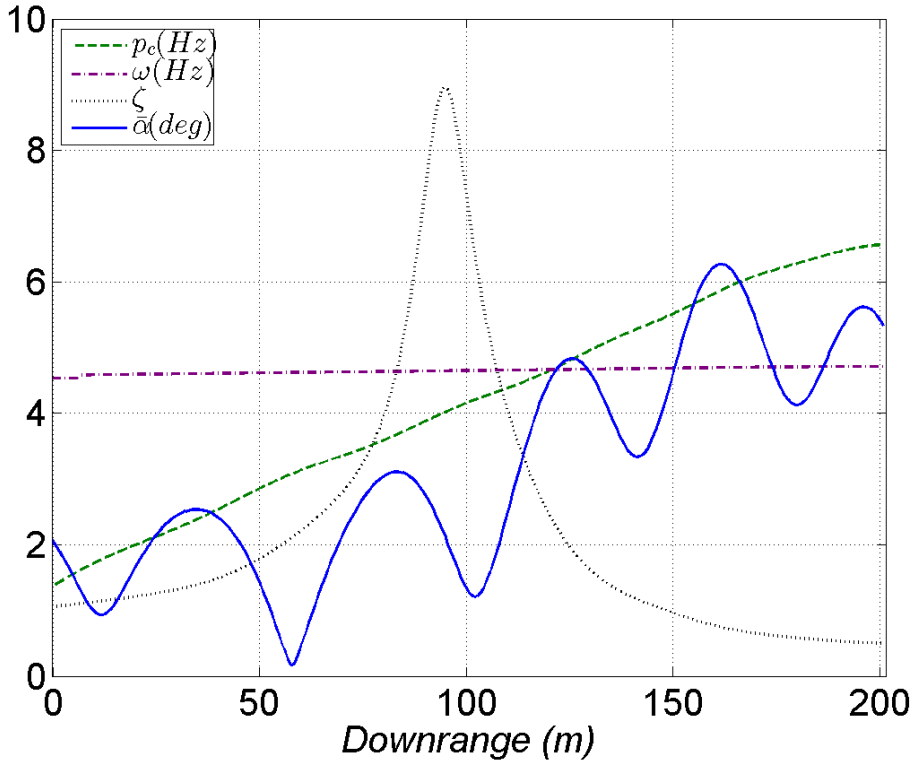

Fig. 14 Resonance for TRN39362

Figure 15 gives the total angle of attack, calculated roll rate, yawing frequency, and amplification factor for TRN39363. These results are consistent with those shown for TRN39362 except the total angle of attack remains below 1°. There appears to be less trim to amplify during roll-yaw resonance for TRN39363. The first maximum yaw is less than one for this flight (over 2° for TRN39362), the amplification peaks at 8 (9 for TRN39362), and the final roll rate is 7 Hz (6.5 Hz for TRN39362). The lower roll rate for TRN 39362 at range exit could be due to transfer of motion from roll to yawing via resonance or just experimental variability. Thus, TRN39362 and TRN39363 undergo different total angle-of-attack histories while exhibiting similar flight dynamic characteristics in many ways.

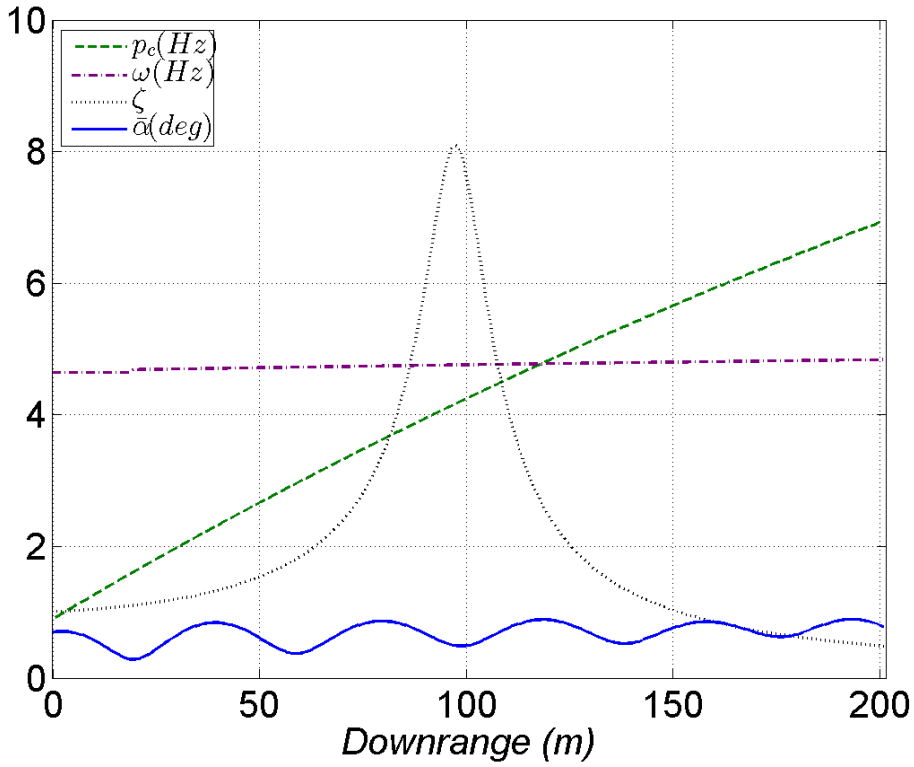

Fig. 15 Resonance for TRN39363

The data in Table 2 was used to determine whether tip-off or trims were more important to the maximum total angle of attack. Figure 16 shows correlations of the maximum total angle of attack with tip-off amplitude (upper left), total aerodynamic asymmetry trim angle (upper right), and trim angle due to mass asymmetry (bottom). The scatter in the upper-left plot of Fig. 16 indicates that tip-off amplitude does not significantly influence the maximum total angle of attack. A weak trend does appear in the upper-right plot, suggesting that the aerodynamic asymmetry trim angle affects the peak yaw. The bottom plot shows that maximum total angle of attack is appreciably influenced by the mass asymmetry (on average by a factor near 4). These data suggest that mass asymmetry most strongly correlated with the peak yaw.

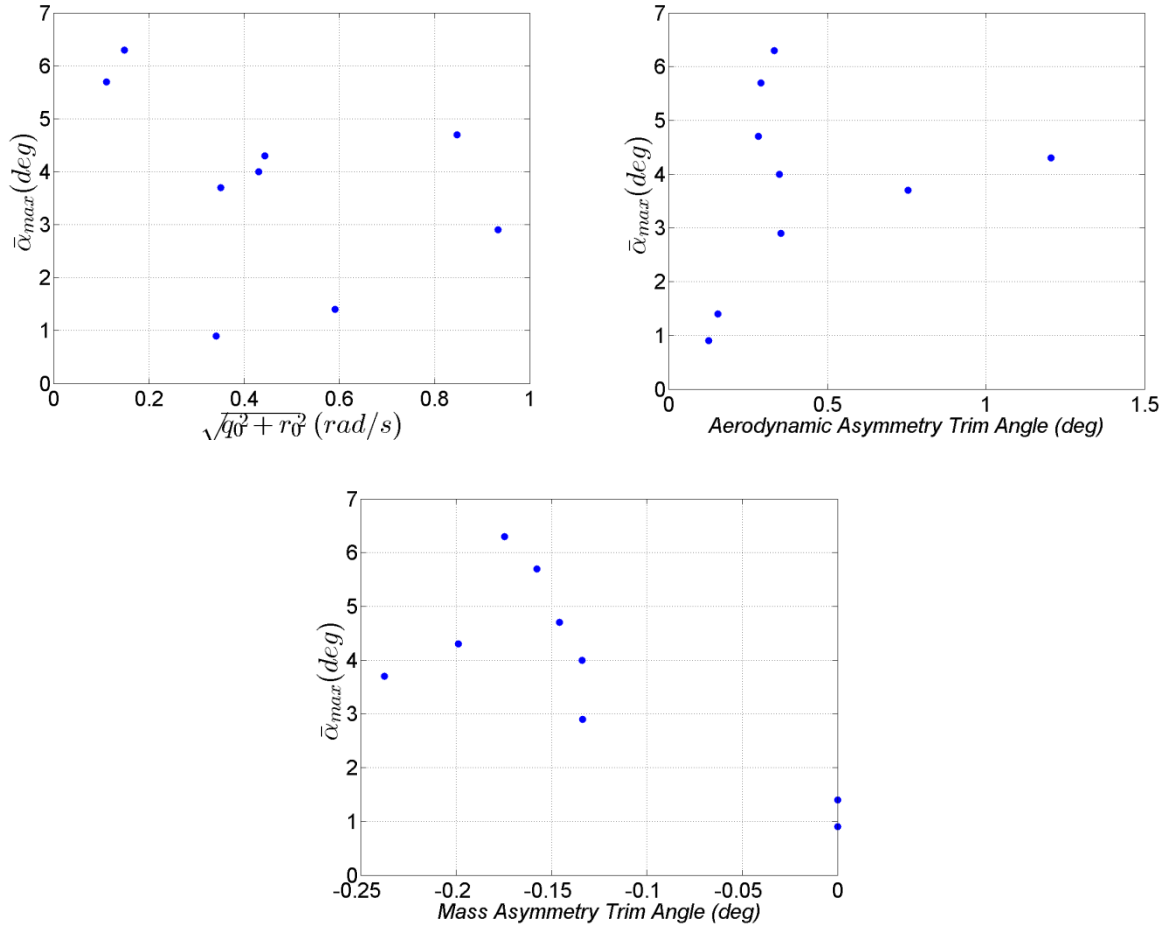

Fig. 16 Correlations between maximum total angle of attack and tip-off, aerodynamic trim, and mass trim

The zero-yaw axial force variation with Mach number is provided in Fig. 17. The blue dots are for the spark range (SR), black line is from the OS technique, and purple squares are for the CFD. The spark range is clustered around Mach 0.9. The average is 0.329 with a 1 standard deviation of 3.7% of the mean. The OS data approximately spans Mach number 0.63 to 0.87 and the Mach number ranged from 0.5 to 1.4 for the CFD. The SR, OS, and CFD data agree favorably.

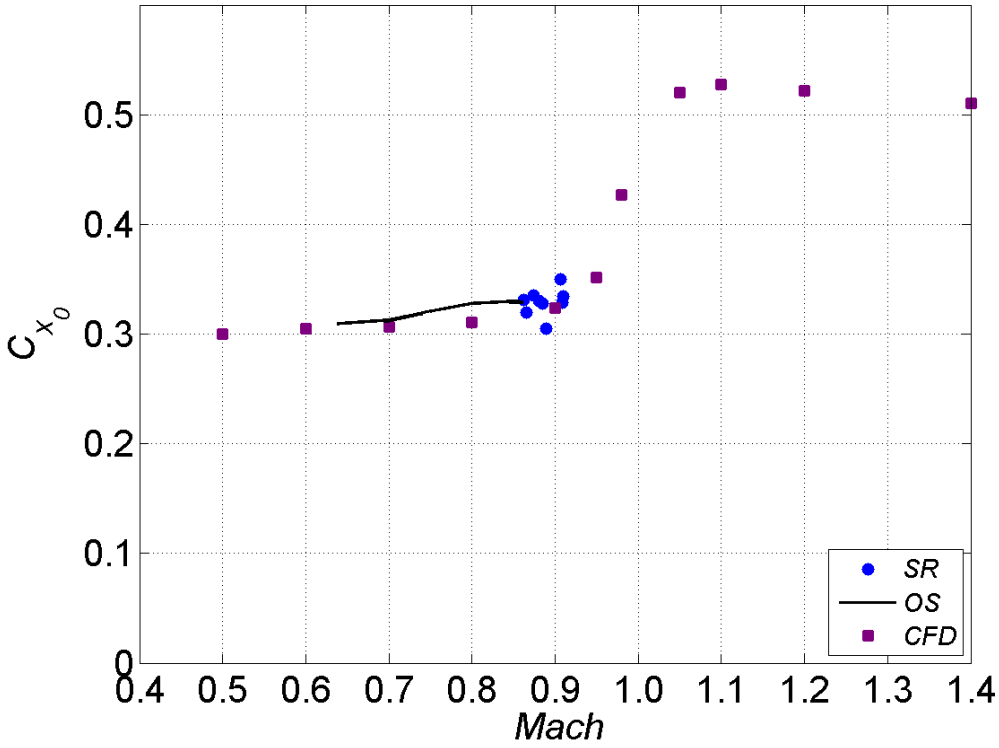

Fig. 17 Zero-yaw axial force coefficient

The pitching moment coefficients are shown in Fig. 18. The blue dots are for SR, lines are for OS, and purple squares for CFD. Filled symbols and solid lines are for the pitching moment coefficient in the yaw plane (canards in the plane, C_{n_β}) and open symbols and dashed lines are for the pitching moment coefficient in the pitch plane (no canards in the plane, C_{m_α}). The dotted line is for OS with a roll-averaged pitching moment ($\bar{C}_{m_\alpha}$) since the separate pitch and yaw plane pitching moments were not able to be determined. The SR results have an average C_{n_β} of –5.68 with a standard deviation of 29% of this mean and an average C_{m_α} of –10.42 with a standard deviation of 11% of the mean. The pitching moments obtained from the internally symmetric models (TRN39045, TRN39363) have larger uncertainty due to lower yaw amplitude. The SR, OS, and CFD pitching moment coefficients compare favorably. The yaw plane pitching moment coefficient for the CFD agrees slightly better with the SR and OS results than the pitch plane pitching moment coefficient.

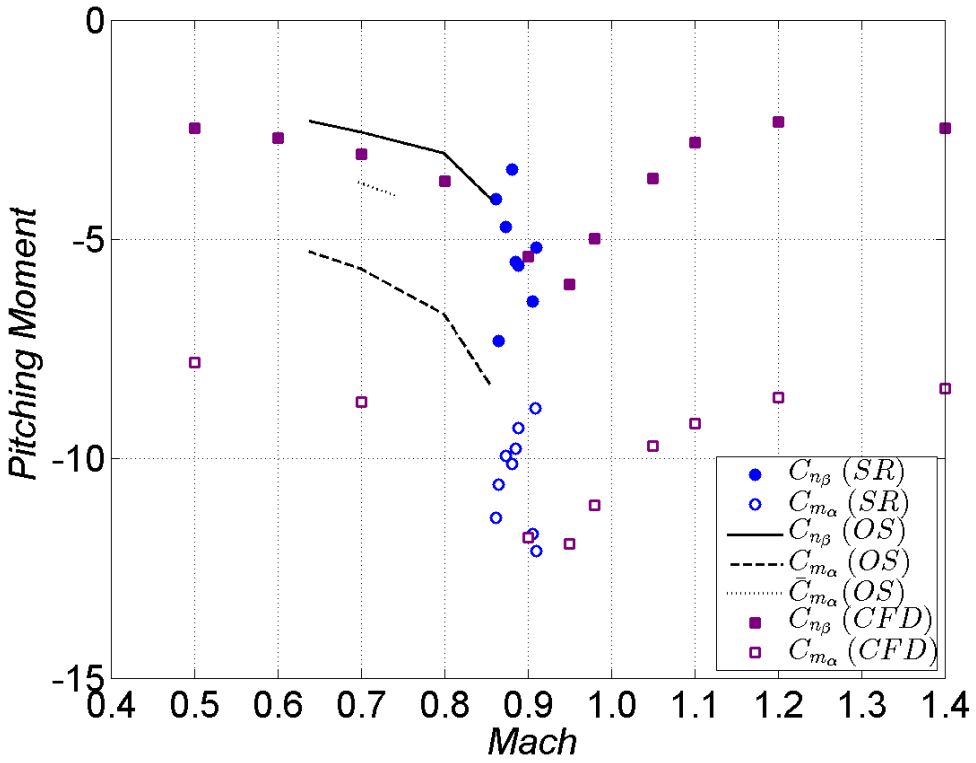

Fig. 18 Pitching moment coefficient

Figure 19 gives normal force coefficients with the same symbols discussed for Fig. 18. The OS technique was only able to obtain an averaged normal force coefficient ($\bar{C}_{N_\alpha}$). The yaw plane normal force coefficient obtained from the spark range had a mean of 8.82 and standard deviation of 14% of the mean. Spark range pitch plane normal force coefficient featured a mean of 6.37 with a standard deviation of 22% of the mean. The canards add slightly more than 2 to the normal force coefficient of the body and fins. The spark range normal force coefficients probably have the highest uncertainty (especially for the low yaw flights) of any aerodynamic coefficients produced from the spark range in this study due to the ratio of the measurement (i.e., altitude and cross-range position) to the measurement error. The SR and CFD results agree for the pitch and yaw plane normal force coefficient. The roll-averaged normal force coefficient from the OS technique lies in the middle of the yaw and pitch plane SR results as expected. The OS results are biased toward the pitch plane normal force coefficients.

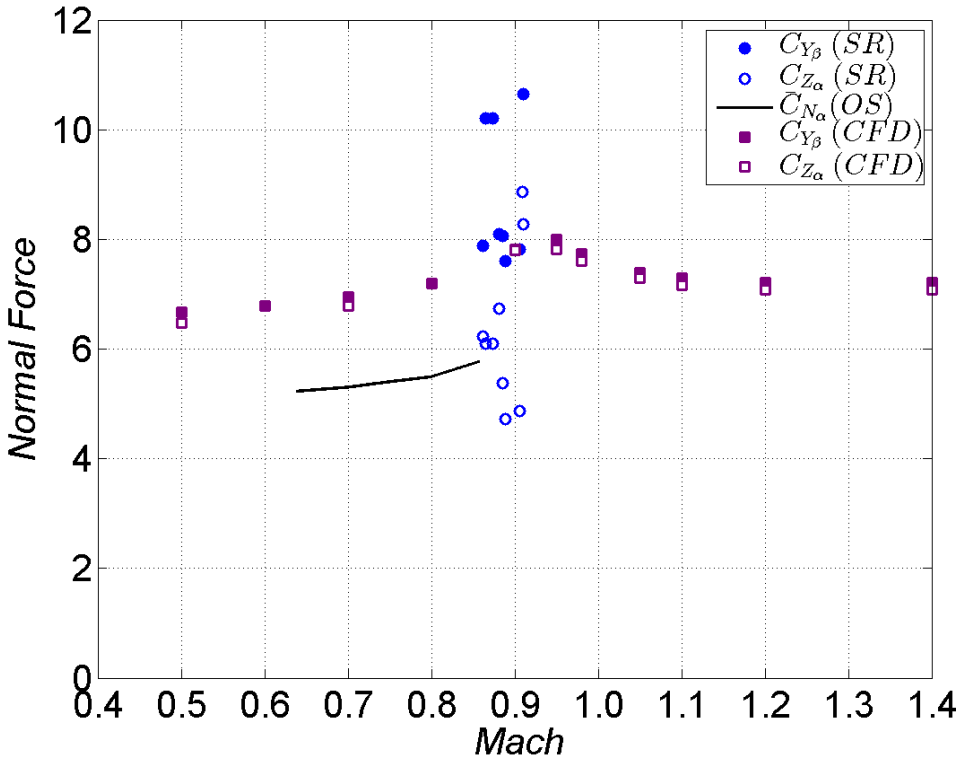

Fig. 19 Normal force coefficient

Aerodynamic center-of-pressure results in the pitch and yaw planes were calculated from the pitching moment and normal force coefficient data and are presented in Fig. 20. SR results put the yaw plane center of pressure 0.65 cal. behind the center of gravity with standard deviation 30% of this mean. The pitch plane center of pressure is 1.70 cal. rearward of the center of gravity with standard deviation 23% of the mean. The pitch and yaw plane center of pressure is similar for the SR, OS, and CFD.

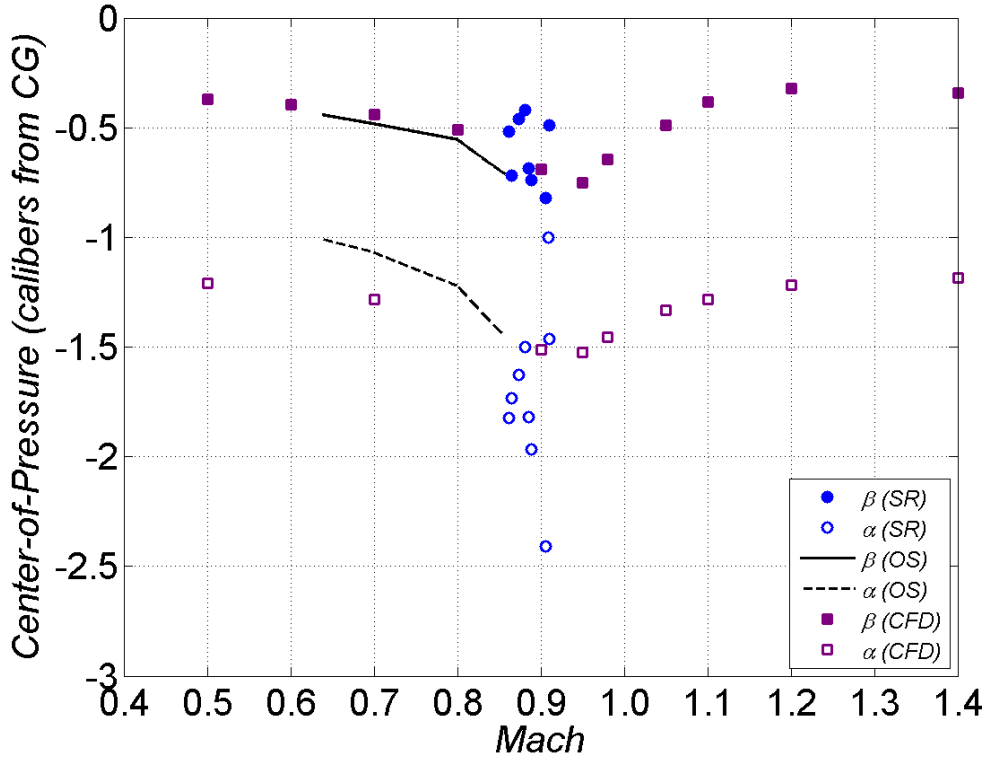

Fig. 20 Center of pressure

The static roll moment coefficients are presented in Fig. 21. The average SR static roll moment coefficient was 0.0506 with standard deviation 9% of the mean. SR, OS, and CFD results compare favorably. The analysis of one of the OS flights featured a strong Mach variation (i.e., larger slope).

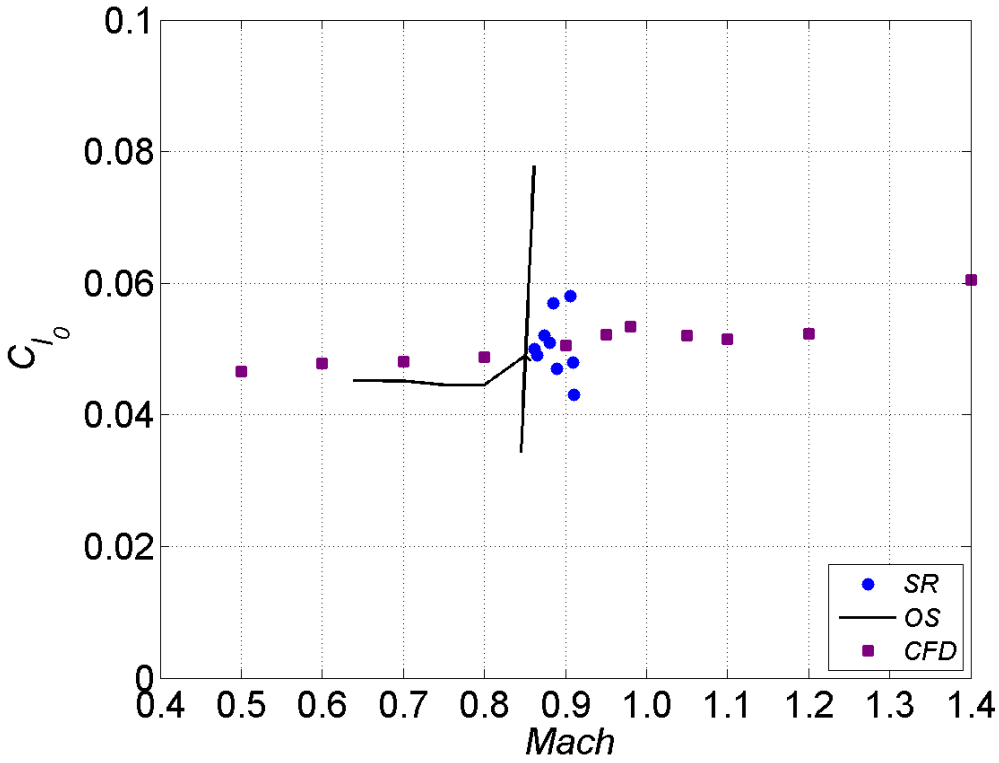

Fig. 21 Static roll moment coefficient

The SR- and OS-based roll damping moment coefficients are shown in Fig. 22. These techniques yield similar values for this coefficient. The mean roll damping moment coefficient was –3 with a standard deviation of 34% of the mean from the SR technique. The pitch damping moment coefficients (roll-averaged or separate yaw and pitch plane) were unable to be explicitly recovered from the spark range data analysis. The yaw growth experienced by the projectile in these experiments was dominated by the mass asymmetry. This made extraction of the aerodynamic damping difficult due to a small Jacobian term (i.e., change in states per change in coefficient). If the aerodynamic damping is of primary concern, different experimental conditions could be generated (e.g., projectile modified to produce more yaw cycles or projectile without internal symmetry and yaw induction near muzzle) for better assessment. Set values of $C_{n_r} = -200$ and $C_{m_q} = -150$, informed from the CFD predictions, were used in the analysis to better obtain other aerodynamic coefficients. Additionally, the fitting for the yaw-squared axial force coefficient did not improve the analysis so a value of $C_{X_{\bar{\alpha}^2}} = 1.35$ was used throughout. A small static side moment was used to improve the analysis for some flights. Dynamic side moments were analyzed but could not be inferred with certainty.

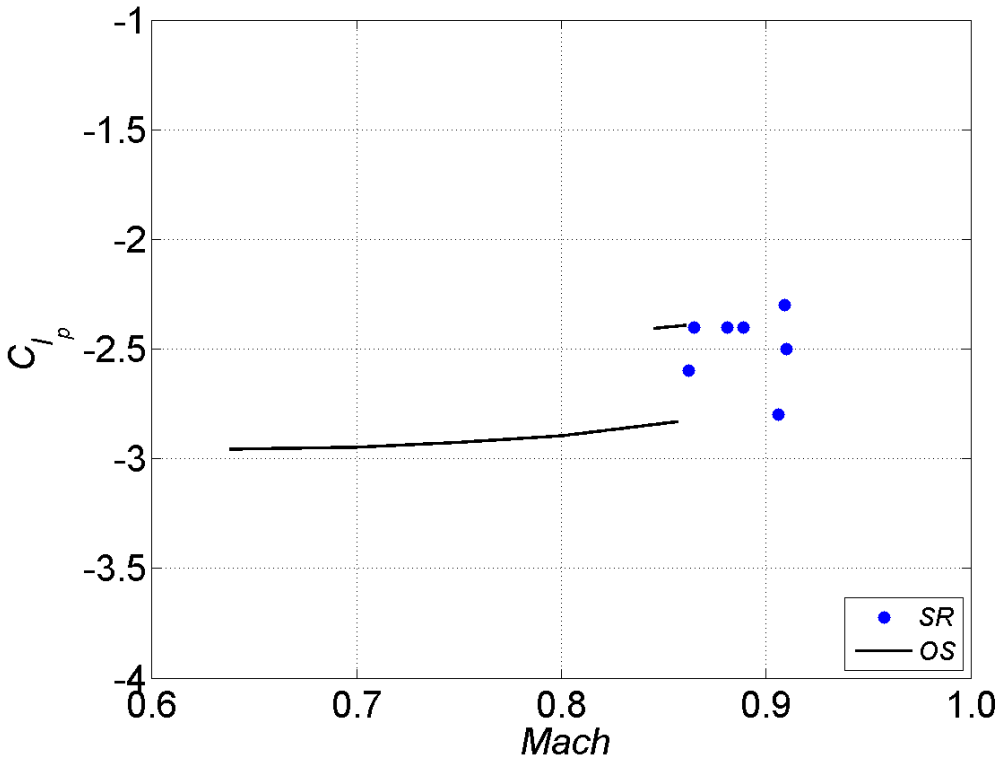

Fig. 22 Roll damping moment coefficient

The airframe under investigation was developed as a vehicle to demonstrate guidance, navigation, and control (GNC) technologies (e.g., low-cost gun-hard control actuation systems, guidance and flight control algorithms, attitude estimation algorithms). The maneuverability was sufficient for demonstration purposes but may not have been optimal. Spark range techniques were applied in this study, along with other aerodynamic methods, to better understand the flight behavior. This exercise permits optimal airframe analysis by considering the uncertainties due to manufacturing variation and modeling accuracy.

Mean and uncertainty in the aerodynamic coefficients were assembled using all aerodynamic data. Inspection of all aerodynamic coefficients provided in this study suggests good agreement among SR, OS, and CFD techniques. Both SR and OS techniques are based on free-flights; however, the aerodynamic parameters are estimated by measured motions and not directly calculated as in CFD or WT techniques. The CFD data compare well with results from SR and OS. This implies good prediction of the integrated surface pressures (i.e., normal force) in addition to faithful representation of the local pressure distribution (i.e., pitching moment, separation/wake near base for axial force) due to turbulence modeling or grid resolution (sometimes more difficult to capture computationally).

The SR results were used for the mean and uncertainty of the aerodynamic coefficients for this airframe. These data were implemented in the 6-degrees-of-freedom model and maximum maneuvers were simulated. The uncertainties were critical in defining the maneuver boundaries. Less static stability and more normal force yields more aggressive maneuvers and more static stability and less normal force results in more moderate maneuvers.

Figure 23 illustrates the total angle of attack (left) and lateral acceleration (right) considering the uncertainty boundaries for the baseline and a more maneuverable configuration. Four flights were simulated with a ±10° canard deflection oscillating at the roll rate with initial velocity of 300 m/s and initial roll rate of 15 Hz (near steady-state roll rate). One case featured the baseline aerodynamics (blue line denoted μ in legend). Two other cases used the uncertainties from the spark range data analysis corresponding to a less stable/more normal force condition (gray dashed line denoted $\mu + \sigma$ in legend) and a more stable/less normal force (black dashed line denoted $\mu - \sigma$ in legend) condition. The last flight used the less stable/more normal force configuration with a 20% increase in canard area/effectiveness (purple dashed-dot line denoted $1.2 \times \mu + \sigma$ in legend) to push the design margin to the limit.

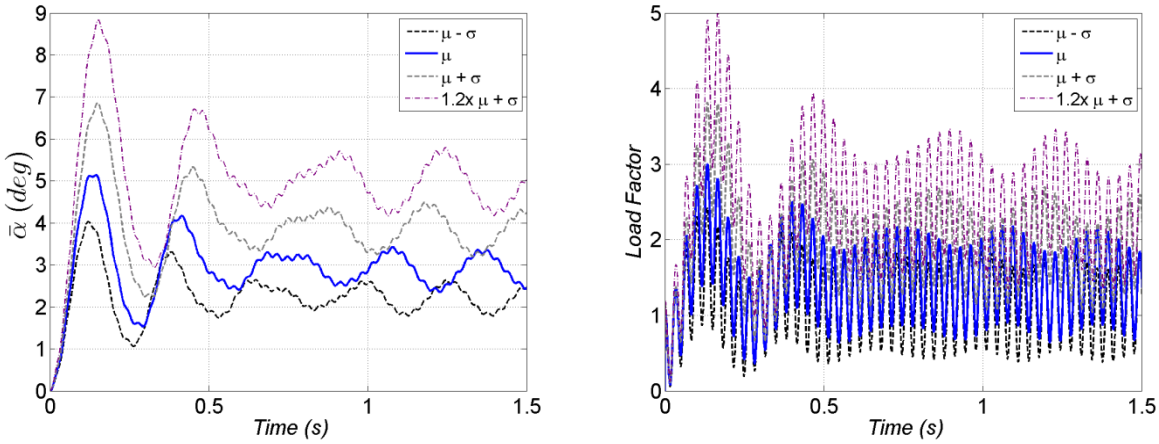

Fig. 23 Effects of uncertainty on maneuverability of baseline and enhanced canard configurations

Some angle-of-attack behaviors are common to all flights. The total angle-of-attack history increases from time zero when the canard deflections start. Angle of attack oscillates at the yaw frequency. Less stable configurations have a lower yawing frequency. Earlier in flight, the angle of attack appreciably overshoots (~170% of steady-state magnitude) and damps with time. All flights have a low amplitude, higher frequency fluctuation at twice the roll rate due to the ±10° canard deflections.

The baseline configuration has a steady-state total angle of attack of about 3°. The uncertainty due to manufacturing tolerances or flight modeling accuracy for the most stable situation produces a steady-state total angle of attack of about 2.3°. When accounting for uncertainties in the least stable case the total angle of attack trims out closer to 3.9°. Thus, when performing maneuvers this airframe most likely flies at 3° but could fly as low as 2.3° and as high as 3.9° when considering one standard deviation uncertainty in the aerodynamics.

This analysis allows investigation of how much more maneuverability margin is available. Steady-state angle of attack increases to about 5° when the canard effectiveness is increased by 20%. Increasing the planform area by roughly 20% or reshaping the airfoil to a more efficient configuration are means of achieving this canard effectiveness. The canard effectiveness could be increased further and still maintain stable flight at a higher angle of attack. However, this invalidates the current aerodynamic model, and additional nonlinearities due to effects such as canard stall need to be investigated further.

The load factor, calculated as the lateral aerodynamic force divided by the weight of the airframe, is presented in the right of Fig. 23 for these 4 cases. The trends in the load factor (e.g., lower frequency oscillation at yawing frequency, higher frequency oscillation at twice the roll rate, overshoot) mimic the total angle-of-attack histories since the aerodynamic forces scale with angle of attack. The load factor oscillation at twice the roll rate is an appreciable percentage of the overall magnitude. This occurs because the local angle of attack at each canard varies 10° plus the body angle of attack (e.g., around 3° for the baseline configuration) over a roll cycle, which yields significant canard normal force variation. The bias around this canard oscillation is due to the body-fin normal force pitched to the body angle of attack.

The baseline configuration average load factor is near 1.4 with canard-induced oscillation of 0.6. The less stable configuration has a load factor of 1.8 ± 0.6 and the more stable configuration has a load factor of 1.1 ± 0.6. If canard effectiveness were enhanced by 20% for the less stable situation, then the load factor improves to 2.4 ± 0.8. These results suggest that this airframe flies with a load factor around 1.4 but one standard deviation uncertainties could change the load factor by as much as 1.8 or as little as 1.1. The variation in load factor due to canard oscillations is a significant percentage of the overall magnitude and increases with canard effectiveness.

4. Conclusions

This study investigated the flight behavior of asymmetric airframes to ultimately provide better guidance performance. Models were designed with internal mass asymmetries with the intent of amplifying yaw through roll-yaw resonance during spark range experiments. The aerodynamic modeling, governing equations for flight, parameter estimation algorithms, and linear theory expressions used in the analysis were described. Spark shadowgraphs were used to reconstruct the flights and obtain aerodynamic coefficients.

The favorable agreement between the spark range measurements and the calculations (especially given the low measurement error in the spark range) validates the aerodynamic models and equations of motion and demonstrates the effectiveness of the parameter estimation algorithm for this configuration. Models with internal asymmetry achieved about a factor of 4 increase in the total angle of attack over the internally symmetric models. Linear theory was applied to show that roll-yaw resonance amplified the trim due to mass asymmetry. Comparing the experimental observations with the linear theory predictions confirmed the theory for this class of asymmetric flight bodies. Analysis of the launch disturbances suggested that angular rates early in flight were produced mainly by the mass asymmetry.

The larger angular motion produced by roll-yaw resonance with the internal asymmetry yielded more accurate aerodynamic coefficients for the body, fin, and canards. The spark range aerodynamic results were similar to the onboard sensor technique and CFD data. This new experimental approach of using internal asymmetries to generate flight motions to better understand the aerodynamics of guided projectiles is a useful tool to aid the development of precision munitions.

Analysis of multiple spark range flights provided some statistical information regarding the uncertainty in the aerodynamics. This uncertainty includes 2 sources: variation due to manufacturing tolerances and flight modeling accuracy. It is difficult to separate the relative magnitude of each at this time. Regardless of the source, the standard deviation in the aerodynamic coefficients was used to evaluate the influence of this uncertainty on the maneuvering flight performance. We compared simulated deflecting-canard flights for the baseline configuration with the less stable/more normal force and the more stable/less normal force. These results showed that the total angle of attack was around 3° with just under ±1° variation due to the aerodynamic uncertainty. Complex behaviors in the

angle-of-attack histories were described previously. The load factor was near 1.4 with about ±0.4 variations from uncertainty. The load factor analysis also illustrated appreciable fluctuation over a roll cycle due to the dithering canards.

This study permitted a postmortem analysis on the airframe developed for GNC demonstration purposes. The data were used to increase the effectiveness of the canards for the less stable/more normal force uncertainty condition to better understand how close the current configuration is to the design margin edge. This exercise showed that there is more than sufficient design margin available to increase maneuverability. Increasing canard effectiveness 20% increased both total angle of attack and load factor by about 30%. A more detailed evaluation of the design margin edge would better account for nonlinear aerodynamics due to effects such as canard stall and flow separation on the body since the airframe flies at higher angle of attack.

5. References

1. Oskay V, Mermagen WH, Bradley J.W. Instrumented drop tests of a slowly rolling parachute payload. Journal of Guidance and Control. 1981;4(3):267–272.

2. Morrison PH, Amberntson DS. Guidance and control of a cannon-launched guided projectile. Journal of Spacecraft and Rockets. 1977;14(6):328–334.

3. Regan FJ, Smith J. Aeroballistics of a terminally corrected spinning projectile. Journal of Spacecraft and Rockets. 1975;2(12):733–738.

4. Moorhead JS. Precision guidance kits (PGKs): improving the accuracy of conventional cannon rounds. Field Artillery. 2007 Jan-Feb:31–33.

5. Grubb ND, Belcher MW. Excalibur: new precision engagement asset in the warfight. Fires. 2008 Oct-Dec:14–15.

6. Fresconi F, Brown T, Celmins I, DeSpirito J, Ilg M, Maley J, Magnotti P, Scanlan A, Stout C, Vazquez E. Very affordable precision projectile system and flight experiments. Proceedings of the 27th Army Science Conference; 2010; Orlando, FL.

7. Ohlmeyer EJ, Fraysse J, Pepitone TR. Guidance, navigation, and control without gyros: a gun-launched munition concept. Guidance, Navigation and Control Conference and Exhibit; 2002 Aug 5–8; Monterey, CA. AIAA Paper 2002-5025.

8. Ilg M. Framework for a software-defined global positioning system (GPS) receiver for precision munitions applications. Aberdeen Proving Ground (MD): Army Research Laboratory (US); 2012 Apr. Report No.: ARL-TR-5976. Also available at http://www.arl.army.mil/www/default.cfm?technical_report=6417.

9. Maley J. Roll orientation from commercial off-the-shelf (COTS) sensors in the presence of inductive actuators. Proceedings of the Institute of Navigation Joint Navigation Conference; 2011 Jun 27–30; Colorado Springs, CO.

10. Rogers J, Costello M, Harkins T, Hamaoui M. Effective use of magnetometer feedback for smart projectile applications. Navigation. 2011;589(3):203–219.

11. Rogers J, Costello M, Hepner D. Roll orientation estimator for smart projectiles using thermopile sensors. Journal of Guidance, Control, and Dynamics. 2011;34(3):688–697.

12. Rogers J, Costello, M. A low-cost orientation estimator for smart projectiles using magnetometers and thermopiles. Navigation. 2012;59(1)9–24.

13. Allik B, Ilg M, Zurakowski R. Ballistic roll estimation using EKF frequency tracking and adaptive noise cancellation. IEEE Transactions on Aerospace and Electronic Systems. 2013;49(4):2546–2553.

14. Fresconi FE. Guidance and control of a projectile with reduced sensor and actuator requirements. Journal of Guidance, Control, and Dynamics. 2011 Nov-Dec;34;(6):1757–1766.

15. Celmins I, inventor. Method and apparatus for correcting the trajectory of a fin-stabilized, ballistic projectile. United States patent US 8,933,383. 2015 Jan 13.

16. Pamadi KB. Aerodynamic considerations for open-loop control of a statically unstable mortar projectile. Journal of Spacecraft and Rockets. 2014;51(5)1576–1586.

17. Fresconi FE, Harkins T. Experimental flight characterization of asymmetric and maneuvering projectiles from elevated gun firings. Journal of Spacecraft and Rockets. 2012;49(6):1120–1130.

18. Ilg M, Fresconi F, Maley J. GPS roll estimation for gun-launched spinning projectiles: hardware-in-the-loop simulation and experimental validation. Proceedings of the Joint Navigation Conference; 2011 Jun 27–30; Colorado Springs, CO.

19. Cooper GR, Fresconi FE, Costello MF. Flight stability of an asymmetric projectile with activating canards. Journal of Spacecraft and Rockets. 2012;49(1):130–135.

20. Fresconi F, Plostins P. Control mechanism strategies for spin-stabilized projectiles. Journal of Aerospace Engineering. 2010;224(G9):979–992.

21. Fresconi FE, Celmins I, Fairfax LD. Optimal parameters for maneuverability of affordable precision munitions. Proceedings of the 50th AIAA Aerospace Sciences Meeting including the New Horizons Forum and Aerospace Exposition 2012; 2012 Jan 9–12; Nashville, TN. Red Hook (NY): Curran Associates, Inc. c2012. Paper No. AIAA-2012-0254.

22. Rogers WK. The transonic free flight range. Aberdeen Proving Ground (MD): Army Ballistic Research Laboratory (US); 1958 Jun. Report No.: BRL-1044.

23. Murphy CH. Data reduction for the free flight spark ranges. Aberdeen Proving Ground (MD): Army Ballistic Research Laboratory (US); 1954 Feb. Report No.: BRL-900.

24. Massey KC, Silton SI. Combining experimental data, computational fluid dynamics, and six-degree of freedom simulation to develop a guidance actuator for a supersonic projectile. Journal of Aerospace Engineering. 2009;223:341–355.

25. Scheuermann E, Costello MF, Silton S, Sahu J. Aerodynamic characterization of a microspoiler system for supersonic projectiles. Journal of Spacecraft and Rockets. 2015;52(1):253–265.

26. Whyte RH, Winchenbach GL, Hathaway WH. Subsonic free-flight data for a complex asymmetric missile. Journal of Guidance and Control. 1981;4(1):59–65.

27. Murphy CH. Free flight motion of symmetric missiles. Aberdeen Proving Ground (MD): Army Ballistic Research Laboratory (US); 1963 Jul. Report No. 1216.

28. Nicolaides J. On missile flight dynamics [PhD dissertation]. [Washington (DC)]: Catholic University of America; 1963.

29. McCoy R L. Modern exterior ballistics: the launch and flight dynamics of symmetric projectiles. Atglen (PA): Schiffer Publishing Ltd; 1999.

30. Pepitone TR, Jacobson ID. Resonant behavior of a symmetric missile having roll orientation-dependent aerodynamics. Journal of Guidance and Control. 1978;1(5):335–339.

31. Celmins I. Sabot concept evaluation using subscale airgun-launched 3-D printed components. Aberdeen Proving Ground (MD): Army Research Laboratory (US); Report No.: ARL-TR-7187. Also available at http://www.arl.army.mil/www/default.cfm?technical_report=7300.

32. Fresconi FE, Celmins I, Silton S. High maneuverability projectile flight using low cost components. Aerospace Science and Technology. 2015;41:175–188.

33. Chapman G, Kirk D. A new method for extracting aerodynamic coefficients from free-flight data. AIAA Journal. 1970;8(4):753–758.

34. Hathaway W, Whyte R. Aeroballistic research facility free flight data analysis using the maximum likelihood method. Eglin Air Force Base (FL): Air Force Armament Laboratory (US); 1979 Dec. Report No.: AFATL-TR-79-98.

35. Iliff K. Parameter estimation for flight vehicles. Journal of Guidance. 1989;12(5):609–622.

36. Klein V, Morelli EA. Aircraft system identification: theory and practice. Reston (VA): AIAA Education Series; 2006.

37. Sahu J, Fresconi FE. Aeromechanics and control of projectile roll using coupled simulation techniques. Journal of Spacecraft and Rockets. 2015;52(3):944–957.

Appendix A. Information on 8-inch Gun Firing 105-mm Projectile in Obturator Assembly-Pusher Plate-Sabot Assembly

The 8-inch gun (Tube #1506) was modified by removing the rifling to create a smoothbore tube with a chamber volume of approximately 1,800 cu. inches based on stargauge measurements conducted by the Aberdeen Test Center. The gun was fixtured to an M174 carriage. An MK2A4 igniter was used with a 7-perforation M2 propellant that was sewn into a bag with a black powder base pad.

The launch package featured an aluminum pusher plate surrounded by a nylon obturator. The projectile was placed on the base assembly (obturator/pusher plate) and the sabot was brought down from over the nose. The nylon sabot had 4 petals and 6 spacer blocks to accommodate the 6 fins. The petals were cut to within about 0.5 inch of the end of the material and 0.75-inch masking tape was wrapped around the sabot/base assembly to hold the entire launch package together for loading. Figure A-1 provides a rendering of the projectile, obturator, pusher plate, and sabot assembly.

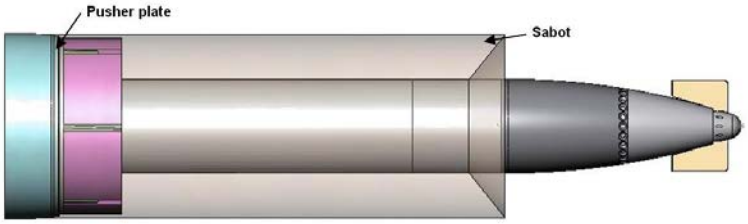

Fig. A-1 Projectile in obturator-pusher plate-sabot assembly

The seating depth was measured about 34 inches when loaded. Fifty-three firings were conducted with this gun and launch package and some relevant launch data are provided below.

Figure A-2 shows the muzzle velocity for 2 in-bore masses (35 and 38.6 kg) with 1.73-kg-charge mass. The lower in-bore mass had a mean velocity of 299.1 m/s with a standard deviation of 10.2 m/s from a sample size of 19. The higher in-bore mass had a mean velocity of 302.2 m/s with a standard deviation of 7.6 m/s from a sample size of 13.

Figures A-3 and A-4 illustrate a linear trend in muzzle energy and chamber pressure with the charge mass from a wider set of firing conditions than that shown in Fig. A-2 (sample size 32).

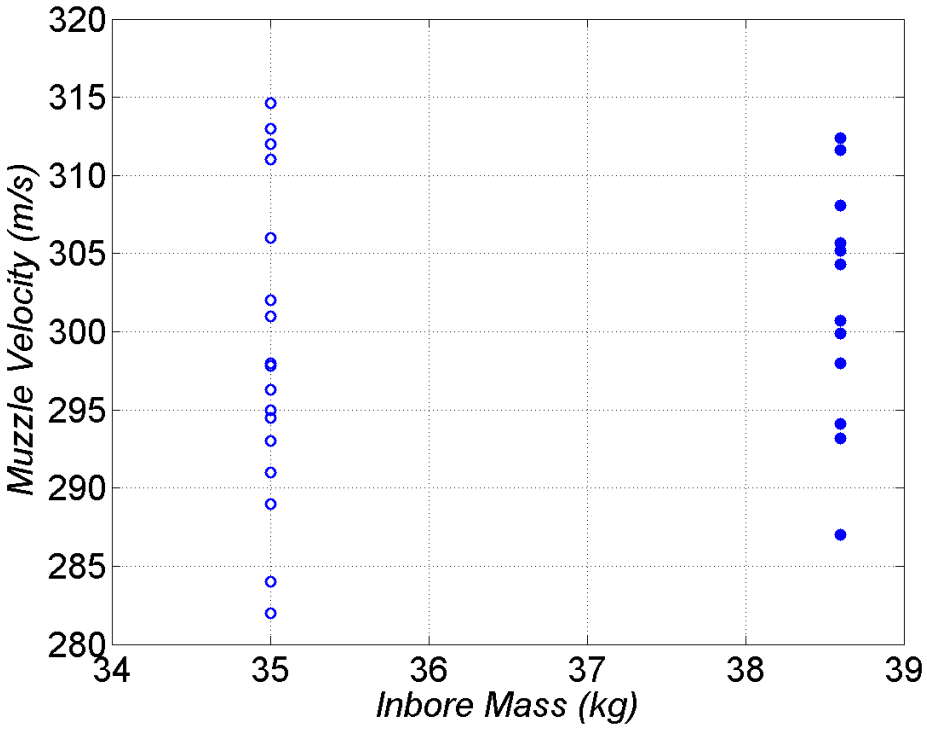

Fig. A-2 Relationship between in-bore mass and muzzle velocity for 1.73 kg of M2 propellant

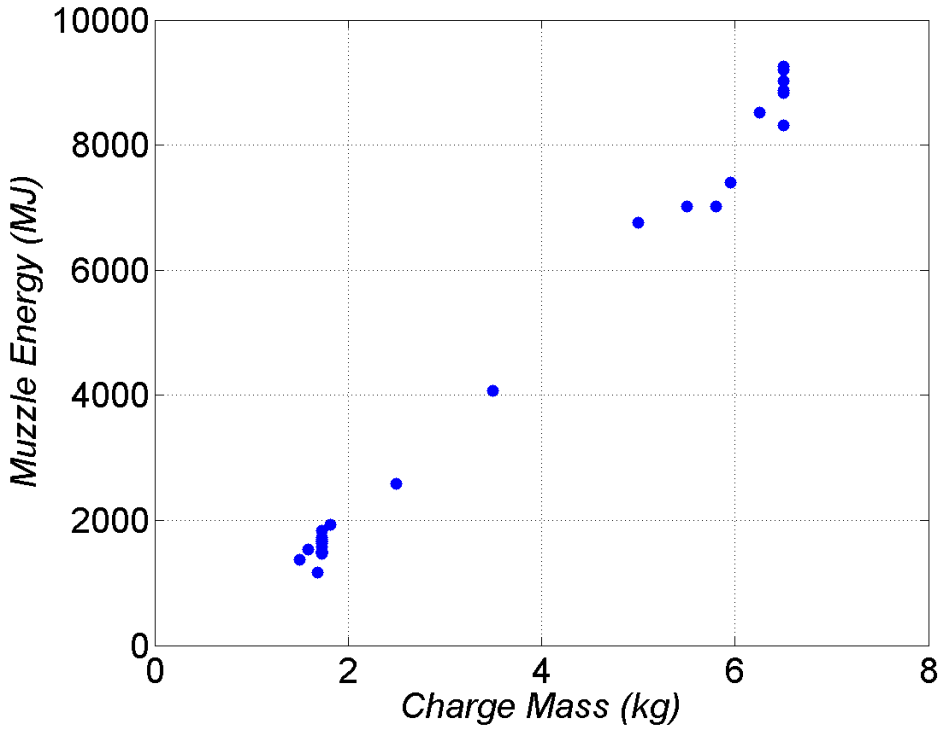

Fig. A-3 Relationship between charge mass and muzzle energy

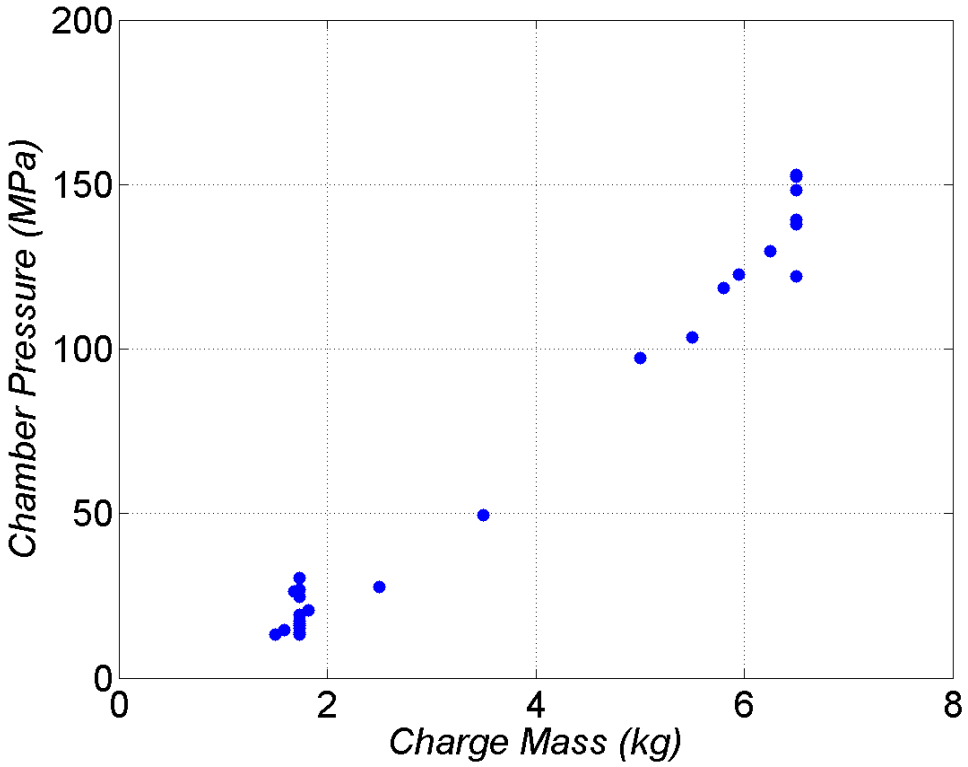

Fig. A-4 Relationship between charge mass and chamber pressure

Appendix B. Asymmetric Mass Properties Measurement Computations

The mass properties of the models were measured on machines at the Transonic Experimental Facility. A high-accuracy scale was used to obtain the mass. The center of gravity and moment of inertia tensor data were collected by precisely placing the models in fixtures with prescribed geometries with respect to the measurement device. These measurement machines (made by Space Electronics) rely on the basic concept of oscillating the model in a single rotational degree of freedom and measuring the angular acceleration and torque to determine the moment of inertia.

The procedure to obtain the center of gravity and moment of inertia tensor for the asymmetric models consisted of collecting a set of data with the longitudinal axis of the model at or nearly parallel to the rotational axis of the machine and a set of data perpendicular to the rotational axis of the measurement machine.

The data collection and analysis with the longitudinal axis of the model at or nearly parallel to the rotational axis of the machine is described first. The initial step is to align the longitudinal axis of the model parallel to the rotational axis of the machine and collect data with these axes coincident. Next, the model was translated such that the longitudinal axis and the rotational axis of the machine were still parallel but now offset by a known distance. It is important that this translation take place on a line contained within the plane of the lateral mass asymmetry. This sequence was repeated multiple times with different offset distances on both sides of the coincident axis configuration (usually about 5–7 points in about 0.04-cal. increments). A least-squares algorithm was used to fit the moment of inertia (I), distance (x), and mass (m) measurements to a model of the form $I = I^* - m(x - x^*)^2$ to determine the axial moment of inertia about the longitudinal axis of the model (I_{XX}) and the lateral center of gravity ($CG_{Y,N}$). An example of these data is shown in Fig. B-1.

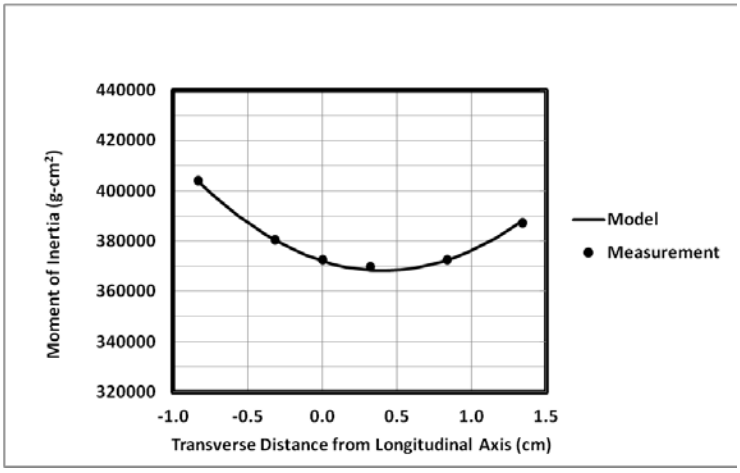

Fig. B-1 Axial moment of inertia about longitudinal axis and lateral center-of-gravity data

The next step in the analysis is undertaken to determine the orientation (i.e., tilt) of the principal axis coordinate system. The models were mounted with a small angle between the longitudinal axis of the model and the rotational axis of the measurement machine. Again, data were collected with the models translated along the axis containing the mass asymmetry. This process was repeated with different tilt angles (γ) (usually about 5–7 angles in about 0.5° increments). These data were fitted to a model of the form $I = I^* - m(\gamma - \gamma^*)^2$ to determine the axial moment of inertia about the principal axis ($\hat{I}_{XX}$) and the tilt angle of the principal axis (γ^*). An example of these data is shown in Fig. B-2.

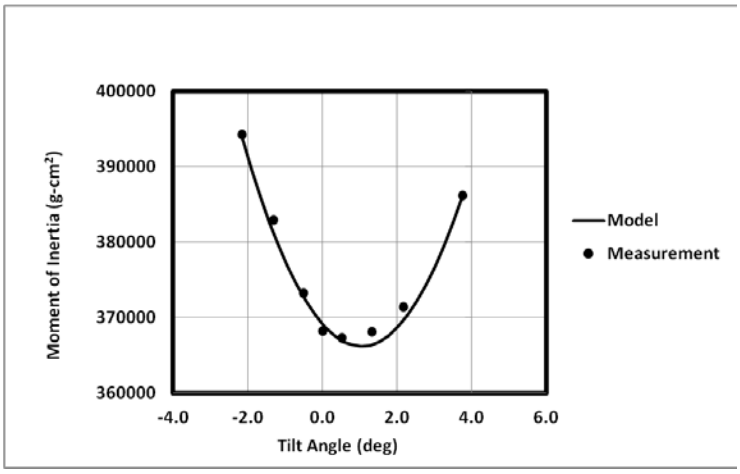

Fig. B-2 Axial moment of inertia about principal axis and tilt angle of principal axis

Next, a series of data was collected with the longitudinal axis of the model perpendicular to the rotational axis of the measurement machines. Two sets of data were collected, one with the rotational axis of machine containing the mass asymmetry and another data set perpendicular to this plane. In each of these planes, multiple data points were collected by translating the model to improve the data quality through the least-squares algorithm. Once more, the moment of inertia (I), distance (x), and mass (m) measurements were fit to a model of the form $I = I^* - m(x - x^*)^2$ to determine the transverse moments of inertia (I_{YY}, I_{ZZ}) and the longitudinal center of gravity ($CG_{X,N}$). An example of these data is shown in Fig. B-3.

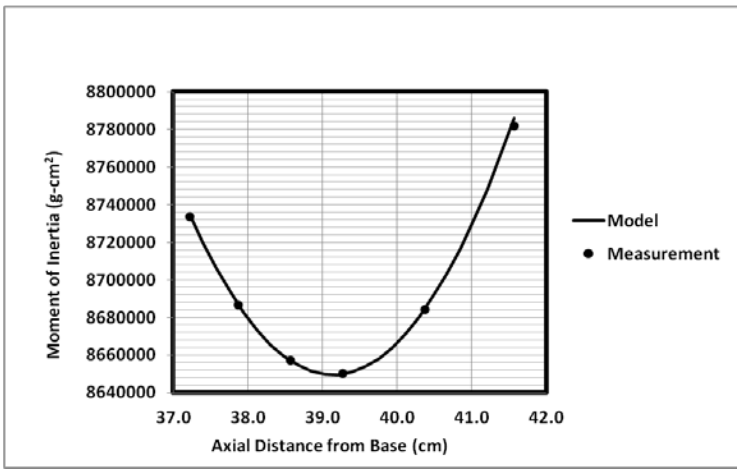

Fig. B-3 Transverse moment of inertia and longitudinal center of gravity

Lastly, the cross-axis moment of inertia was calculated from the tilt angle and transverse and axial moments of inertia through the following expression to completely characterize the internal model asymmetry.

$$I_{XY} = \frac{I_{YY} - I_{XX}}{2} \tan 2\gamma \ . \qquad \text{(B-1)}$$

Appendix C. Measured and Calculated Flight Motion

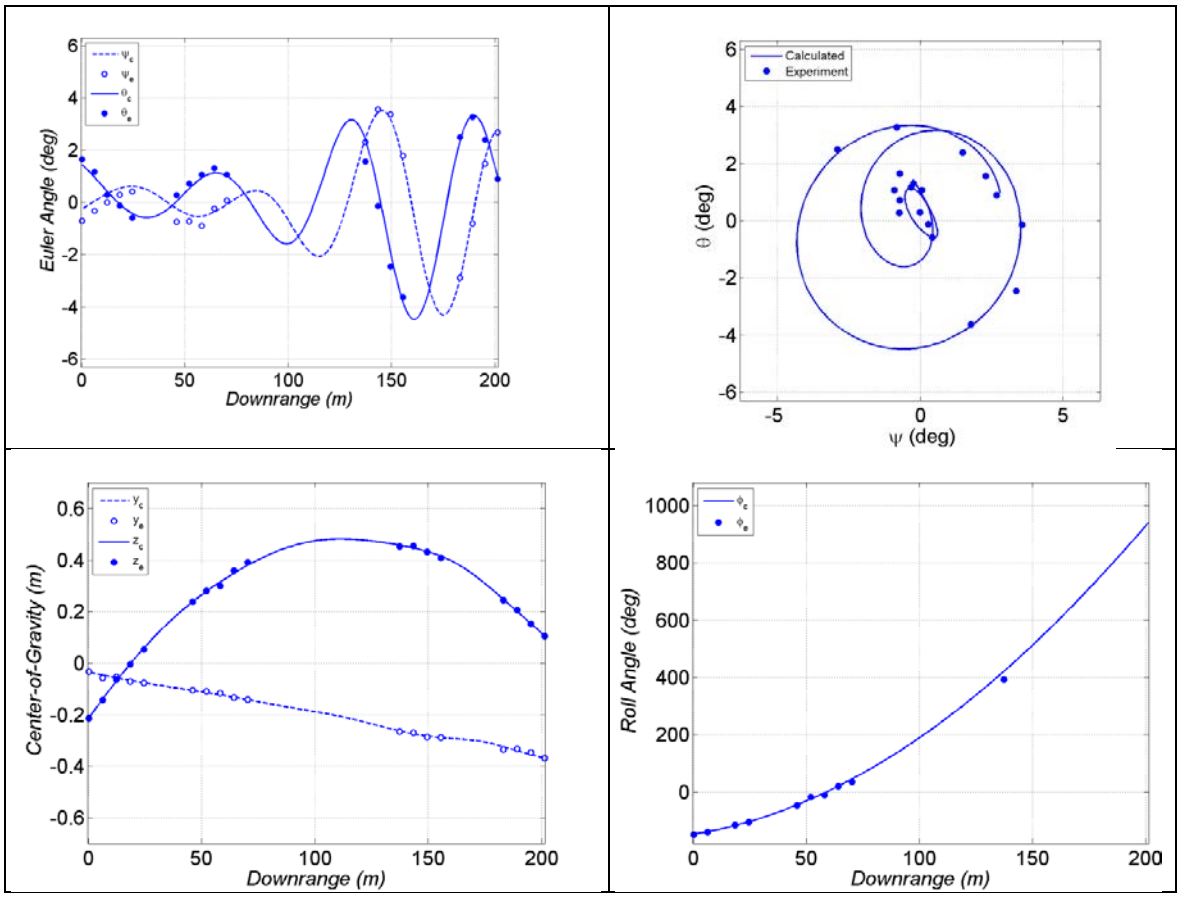

Fig. C-1 Measured and calculated motion for TRN39043

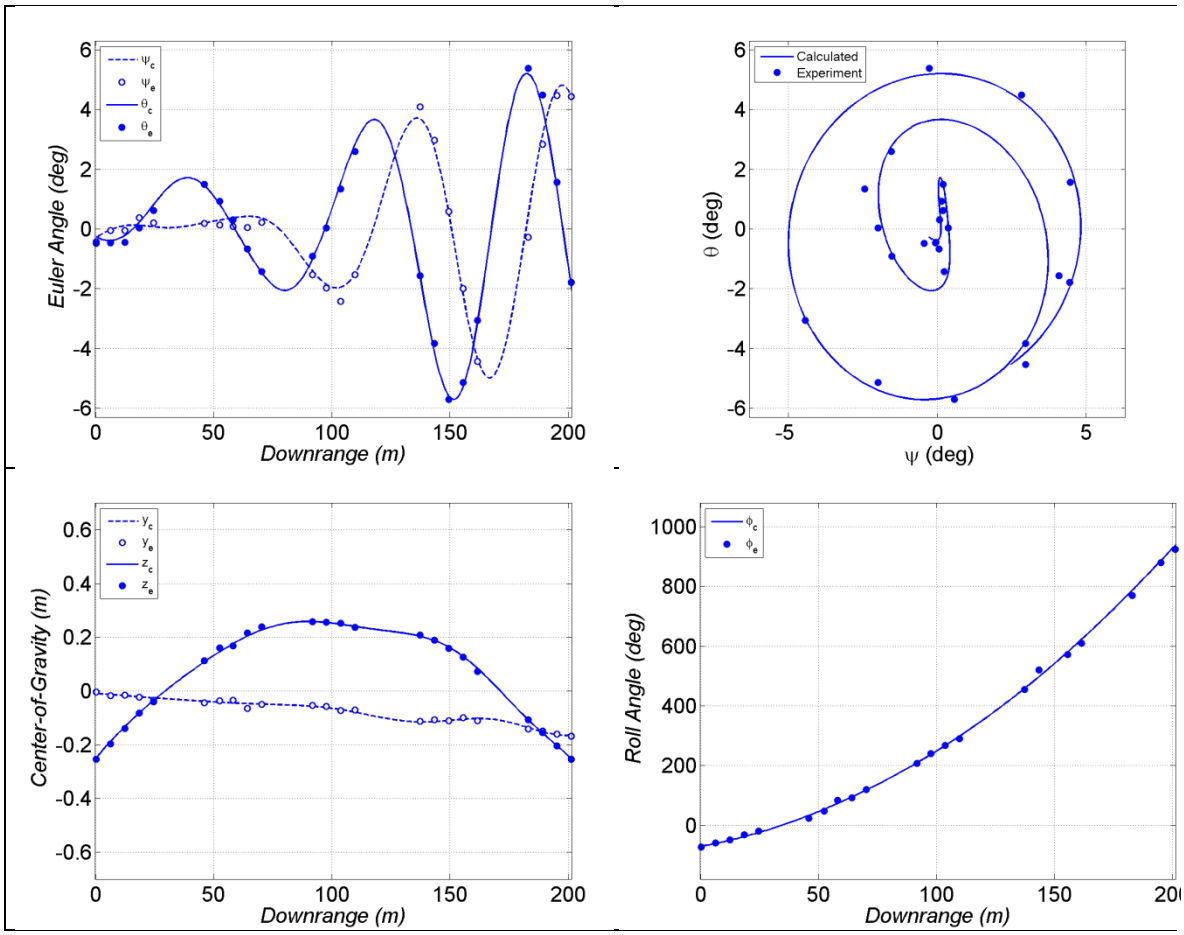

Fig. C-2 Measured and calculated motion for TRN39044

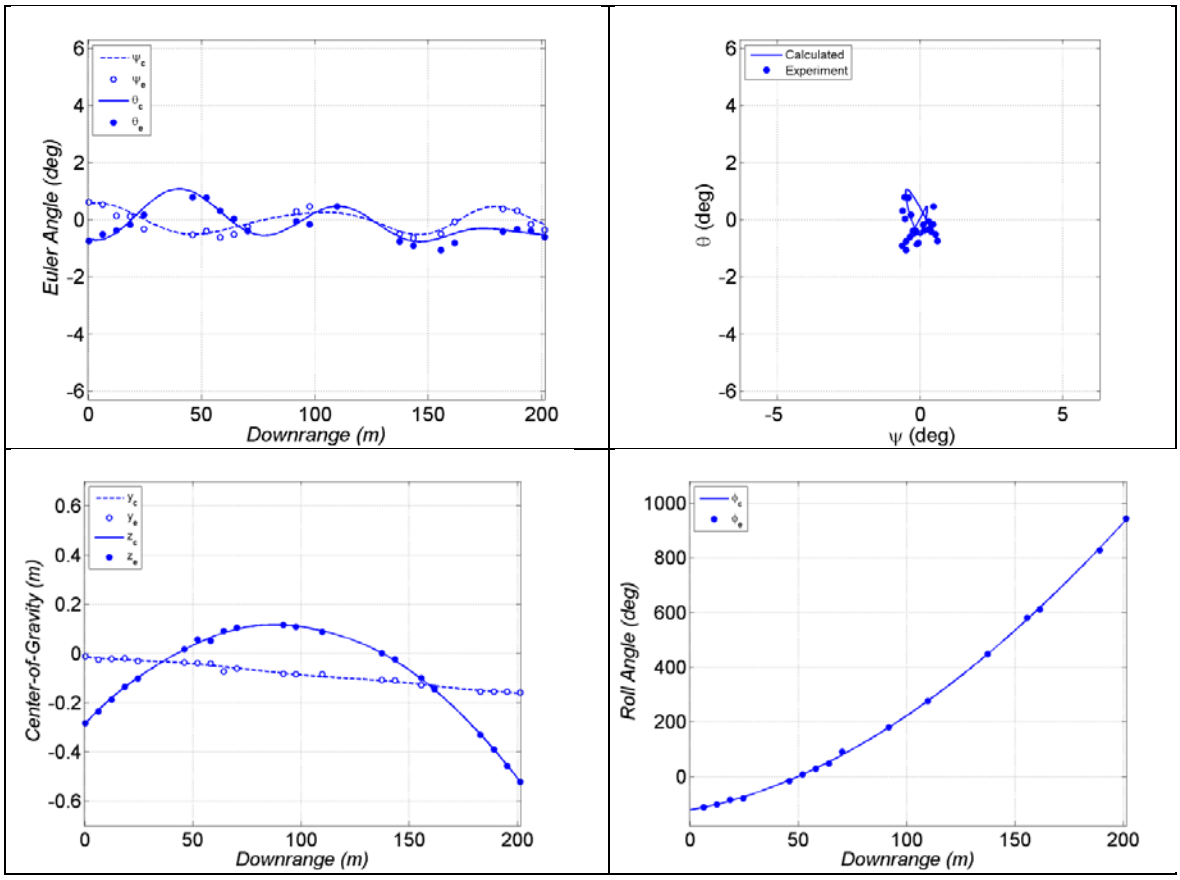

Fig. C-3 Measured and calculated motion for TRN39045

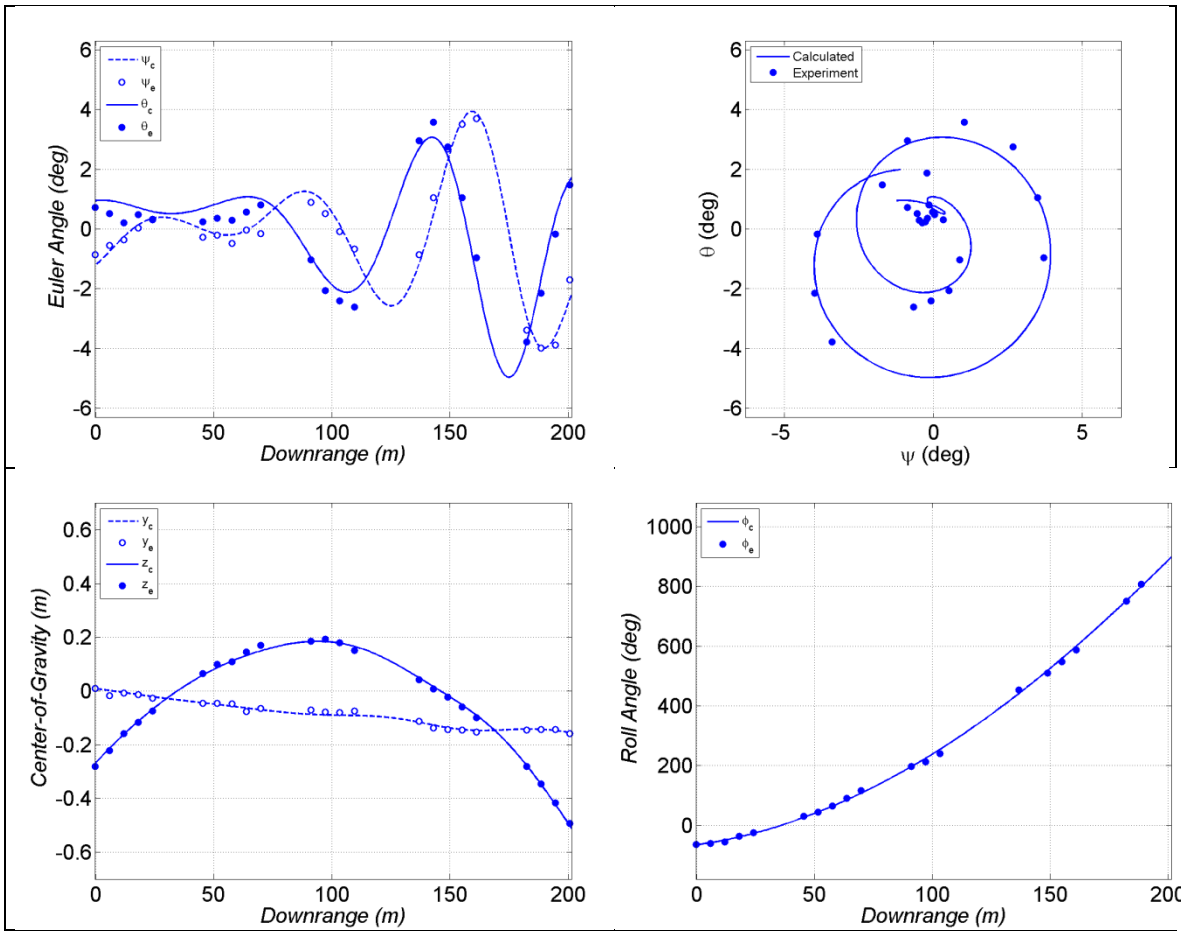

Fig. C-4 Measured and calculated motion for TRN39319

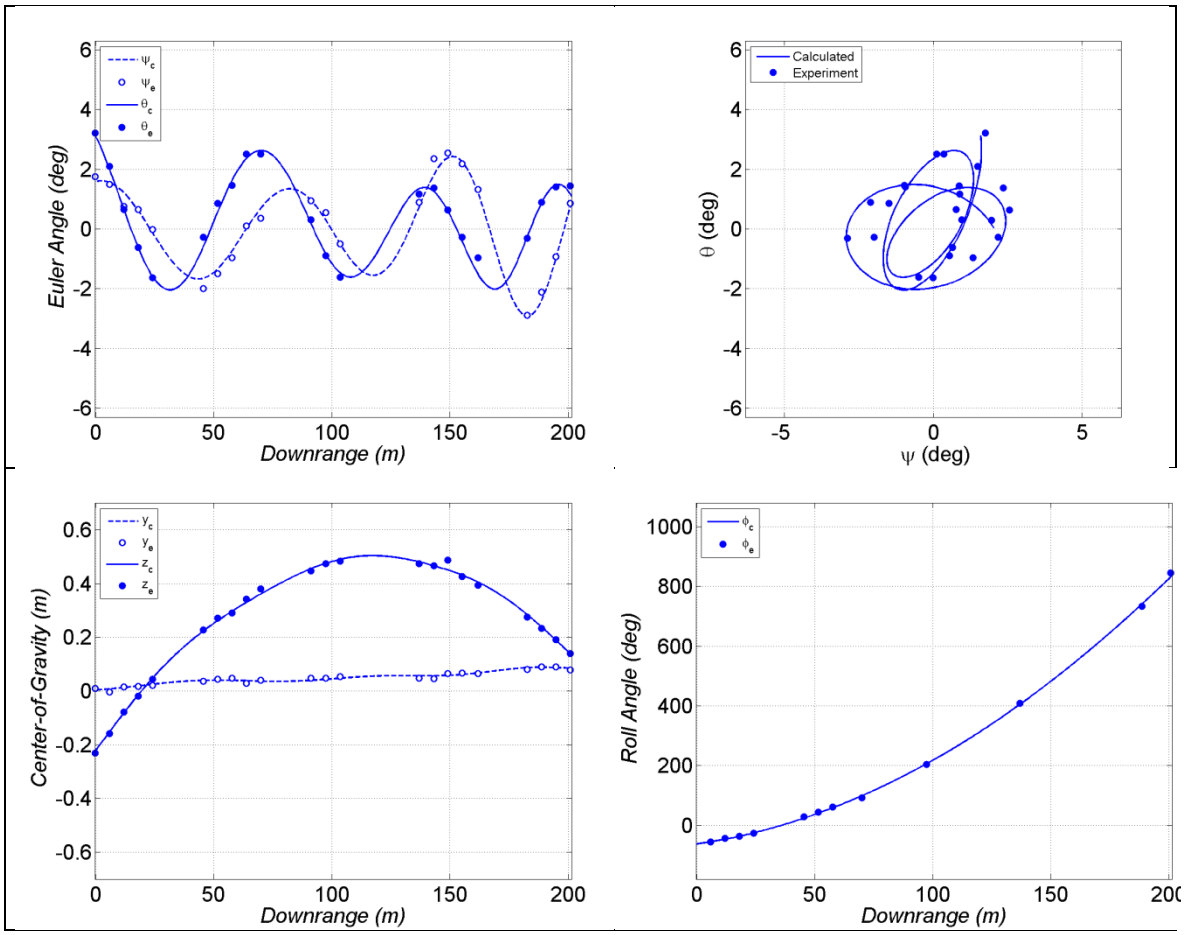

Fig. C-5 Measured and calculated motion for TRN39320

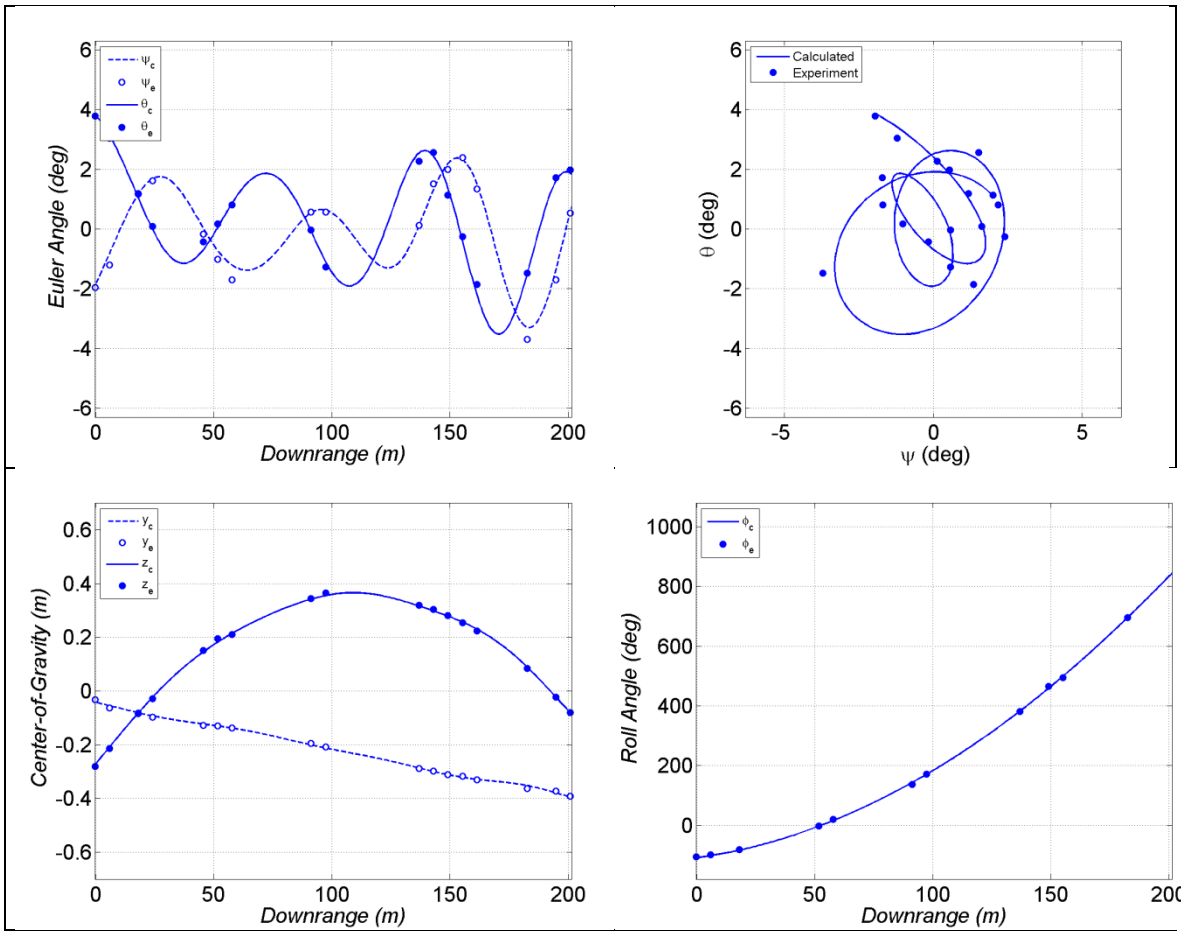

Fig. C-6 Measured and calculated motion for TRN39360

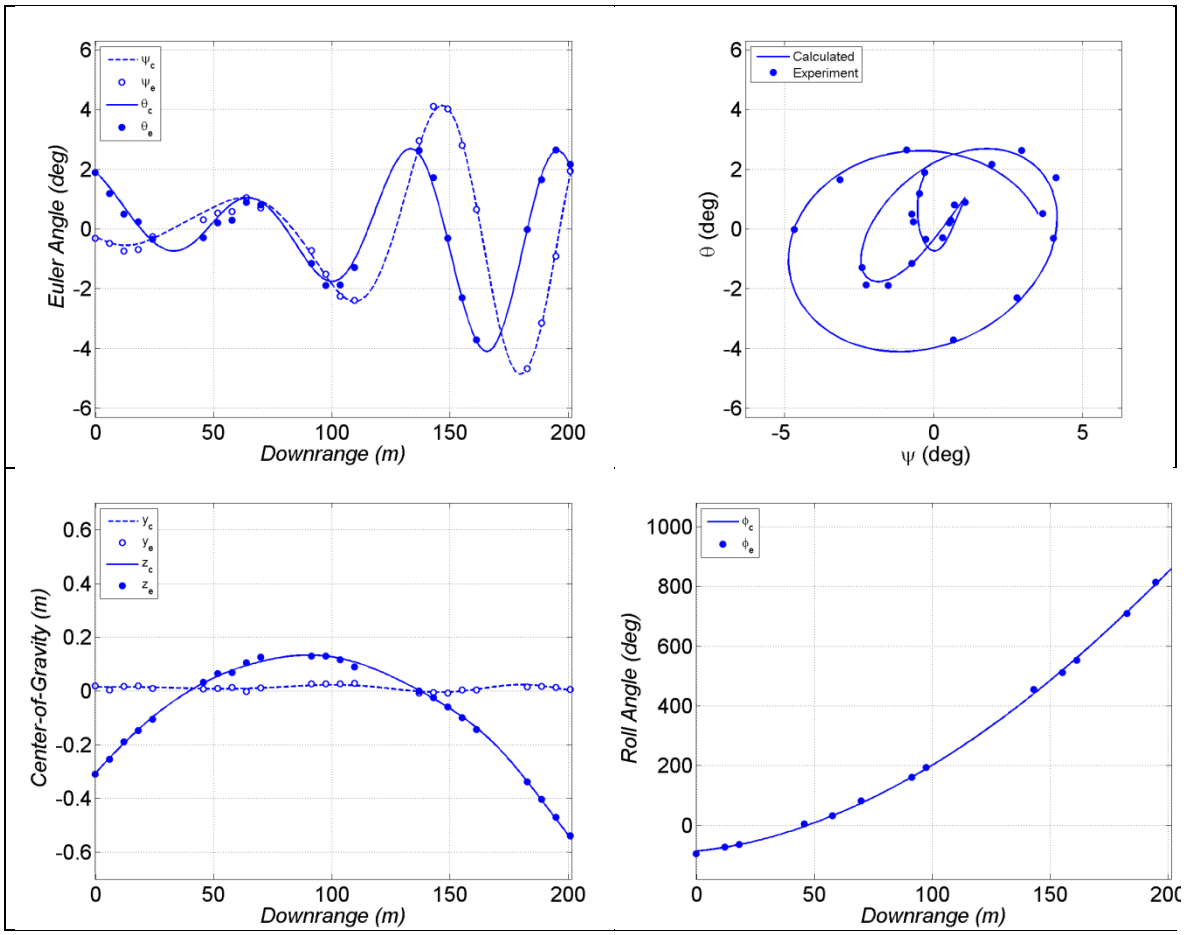

Fig. C-7 Measured and calculated motion for TRN39361

List of Symbols, Abbreviations, and Acronyms

ARL	US Army Research Laboratory
CFD	computational fluid dynamics
GNC	guidance, navigation, and control
OS	onboard sensor
SEAP	semi-empirical aeroprediction
SR	spark range
WT	wind tunnel

1 (PDF)	DEFENSE TECHNICAL INFORMATION CTR DTIC OCA
2 (PDF)	DIRECTOR US ARMY RESEARCH LAB RDRL CIO LL IMAL HRA MAIL & RECORDS MGMT
1 (PDF)	GOVT PRINTG OFC A MALHOTRA
1 (PDF)	ARO S STANTON M MUNSON
9 (PDF)	RDECOM AMRDEC L AUMAN D CHAMNESS J DOYLE S DUNBAR B GRANTHAM J LOCKER M MCDANIEL C ROSEMA M TURNER
1 (PDF)	RDECOM ECBC D WEBER
42 (PDF)	RDECOM ARDEC M BAKER G BISCHER D CARLUCCI J CHEUNG S CHUNG D CLER B DEFRANCO D DEMELLA M DUCA P FERLAZZO G FLEMING R FULLERTON R GORMAN R GRANITZKI N GRAY J GRAU M HOHIL M HOLLIS R HOOKE W KOENIG A LICHTENBERG-SCANLAN S LONGO E LOGSDON M LUCIANO P MAGNOTTI G MALEJKO S MARHEVKA M MARSH G MINER J MURNANE M PALATHINGAL D PANHORST A PIZZA J ROMANO T RECCHIA G SCHLENK B SMITH C STOUT W TOLEDO E VAZQUEZ L VO C WILSON
2 (PDF)	PEO AMMO C GRASSANO P MANZ
2 (PDF)	PM CAS P BURKE M BURKE
1 (PDF)	MCOE A WRIGHT
2 (PDF)	ONR P CONOLLY D SIMONS
4 (PDF)	NSWCDD L STEELMAN K PAMADI H MALIN J FRAYSSE
2 (PDF)	NAWCWD P CROSS R SCHULTZ
3 (PDF)	NAVAIR D FINDLAY J LEE T SHAFER
1 (PDF)	AFOSR EOARD G ABATE
1 (PDF)	MARCORSYSCOM P FREEMYERS

2 (PDF) DARPA
J DUNN
K MASSEY

1 (PDF) NASA
S VIKEN

1 (PDF) DRAPER LAB
G THOREN

1 (PDF) GTRI
A LOVAS

3 (PDF) ISL
C BERNER
S THEODOULIS
P WERNERT

2 (PDF) DRDC
D CORRIVEAU
N HAMEL

3 (PDF) DSTL
T BIRCH
R CHAPLIN
B SHOESMITH

3 (PDF) DSTO
S HENBEST
M GIACOBELLO
B WOODYAT

2 (PDF) GEORGIA INST OF TECH
M COSTELLO
J ROGERS

1 (PDF) ROSE-HULMAN INST OF TECH
B BURCHETT

1 (PDF) AEROPREDICTION INC
F MOORE

1 (PDF) ARROW TECH
W HATHAWAY

1 (PDF) MARTEC LIMITED
D ALLEXANDER

2 (PDF) ATK
R DOHRN
S OWENS

3 (PDF) BAE
B GOODELL
P JANKE
O QUORTRUP

1 (PDF) GD OTS
D EDMONDS

3 (PDF) UTAS
P FRANZ
S ROUEN
M WILSON

1 (PDF) RMS
A VANDERWYST

1 (PDF) STA
D MAURIZI

56 (PDF) DIR USARL
RDRL VTA
C KRONINGER
RDRL VTV
B GLAZ
RDRL WM
P BAKER
RDRL WML
P PEREGINO
M ZOLTOSKI
RDRL WML A
M ARTHUR
W OBERLE
L STROHM
RDRL WML B
N TRIVEDI
RDRL WML C
S AUBERT
RDRL WML D
R BEYER
A BRANT
J COLBURN
P CONROY
M NUSCA
Z WINGARD
RDRL WML E
V BHAGWANDIN
I CELMINS
J DESPIRITO
L FAIRFAX
F FRESCONI
J GARNER
B GUIDOS
R KEPPINGER
G OBERLIN
T PUCKETT
J SAHU

S SILTON
P WEINACHT
RDRL WML F
B ALLIK
T BROWN
E BUKOWSKI
B DAVIS
M DON
D EVERSON
M HAMAOUI
M ILG
B KLINE
J MALEY
C MILLER
P MULLER
B NELSON
B TOPPER
RDRL WML G
M BERMAN
M CHEN
W DRYSDALE
M MINNICINO
J SOUTH
RDRL WML H
T EHLERS
C MEYER
J NEWILL
R PHILABAUM
B SCHUSTER
R SUMMERS
RDRL WMM
J ZABINSKI
RDRL WMP
D LYON